metals

MDPI

Article

Experimental Investigation of Stress Concentration and Fatigue Behavior in 9% Ni Steel Welded Joints under Cryogenic Conditions

Yu-Yao Lin [1], Sang-Woong Han [2], Young-Hwan Park [3] and Do Kyun Kim [1,2,*]

[1] Department of Naval Architecture and Ocean Engineering, College of Engineering, Seoul National University, 1 Gwanak-ro, Gwanak-gu, Seoul 08826, Republic of Korea
[2] Research Institute of Marine Systems Engineering, Department of Naval Architecture and Ocean Engineering, Seoul National University, 1 Gwanak-ro, Gwanak-gu, Seoul 08826, Republic of Korea
[3] Welding & Joining Research Group, POSCO, 6261, DongHaean-ro, Pohang 37859, Republic of Korea
* Correspondence: do.kim@snu.ac.kr

Abstract: This experimental study delves into the intricate mechanics of stress concentration and fatigue behavior exhibited by 9% Ni steel welded joints under cryogenic conditions. The study specifically examines butt-welded, fillet longitudinal, and fillet transverse specimens, comparing their fatigue properties under room and cryogenic temperatures. Notably, determining hot-spot stress presents a challenge, as it cannot be directly obtained through traditional means. To overcome this limitation, a method for predicting hot-spot stress is introduced, which considers the effects of misalignments and weld bead characteristics. The study also highlights the impact of grip-clamping-induced specimen deformation and the reduced middle section on stress concentration resulting from misalignments. Furthermore, it proposes separate consideration of the effects of the weld bead on the axial nominal stress and on the bending stress of the specimen. The accuracy of strain gauge measurements in cryogenic environments is addressed by suggesting a method to correct the output of 2-wire strain gauges using a fixed ratio derived from 2-wire and 3-wire strain gauges. By comparing predicted hot-spot stress with actual measurements, the study validates the reliability of the proposed predictive method. These findings contribute to a deeper understanding of the behavior of 9% Ni steel welded joints under cryogenic conditions and provide valuable insights for design and engineering in similar applications.

Keywords: 9% Ni steel; cryogenic temperature; butt-welded specimen; hot-spot stress; stress concentration factor

check for updates

Citation: Lin, Y.-Y.; Han, S.-W.; Park, Y.-H.; Kim, D.K. Experimental Investigation of Stress Concentration and Fatigue Behavior in 9% Ni Steel Welded Joints under Cryogenic Conditions. *Metals* **2024**, *14*, 741. https://doi.org/10.3390/met14070741

Academic Editor: Qingsong Mei

Received: 29 May 2024
Revised: 17 June 2024
Accepted: 20 June 2024
Published: 22 June 2024

Copyright: © 2024 by the authors. Licensee MDPI, Basel, Switzerland. This article is an open access article distributed under the terms and conditions of the Creative Commons Attribution (CC BY) license (https://creativecommons.org/licenses/by/4.0/).

1. Introduction

Due to the expansion of the global population and economy, there is a concurrent increase in energy demand. This increase in energy needs, combined with the desire to reduce CO_2 emissions, leads to a continuously increasing demand for Liquefied Natural Gas (LNG), which is a clean energy source [1]. As IMO environmental regulations [2], such as CO_2 emission restrictions, have been strengthened, the demand for LNG fuel ships that can replace conventional ships has been increasing. LNG tanks present a potential risk of leakage and explosion accidents, and many researchers have evaluated their safety during cryogenic service [3,4]. The Self-supporting Prismatic shape IMO type B (SPB) LNG tank can reduce the sloshing effect, making it commonly used in LNG fuel ships [5]. The SPB-type tank is mainly made using 9% Ni steel, since 9% Ni steel has excellent mechanical properties under cryogenic temperature [5]. For 9% Ni steel, various monotonic tensile tests and fatigue tests have been conducted recently [6–9].

Shielded metal arc welding (SMAW) and submerged arc welding (SAW) are mainly applied to the welding method for 9% nickel steel. In the case of flux-cored arc welding

(FCAW), welding consumables for 9% nickel steel were developed [9]. Lee et al. found that when the temperature decreased, for 9% Ni steel, no visible improvement in the true tensile strain of the base metal was observed, but a significant increase in the true tensile strain of the weld metal was observed [6]. According to the crack growth and CTOD evaluation, 9% Ni steel did not show any significant change in its mechanical behavior with respect to the temperature drop [6]. In the study by Kim et al., it was noted that as the temperature decreased, the fatigue limits of the base metal, weld metal, and corner weld of 7% nickel steel all increased [7]. The fatigue crack propagation properties of 9% Ni steel were summarized by Shiratsuchi and Osawa [8].

Estimating the fatigue life according to the S-N curve has always attracted attention. There are different approaches for the fatigue life analysis of a welded joint. These methods are distinguished mainly by the parameters used to describe fatigue life "N" or fatigue strength [10]. When performing a series of fatigue tests, the nominal stress can be simply calculated from the dimensions of the specimen and the applied force. The fatigue strength is determined by comparing the nominal stress range with the S-N curves classified according to the weld joint types [11]. The residual stress will affect fatigue properties as well. Xin, H. reported that the full range of S-N curves based on hardness measurements without considering residual stress effects overestimates the fatigue life of butt-welded joints [12]. For the evaluation of stresses in welded joints, hot-spot stresses have been widely used [13]. On the other hand, once the hot-spot stress is considered, the test data would show a significantly improved correlation with the mean S-N curve scatter band [14]. To determine hot-spot stress, strain gauges are typically employed for measurement. Hot-spot stress is estimated by extrapolating values measured from these strain gauges. However, issues such as strain gauge detachment during testing and errors due to improper installation may arise. When working with thin specimens, the short distance between strain gauges and the weld bead complicates accurate installation. Especially in the case of cryogenic temperature experiments, the accuracy of the strain gauge would be degraded. This study aims to overcome these challenges by developing precise and efficient methods for detecting hot-spot stress in cryogenic environments.

The stress concentration factor (*SCF*) is defined as the ratio of the maximum stress to the nominal stress of a target section. In the case of butt-welded joints, to address the practical issues, the stress concentration factor is used as the ratio between the hot-spot stress and the nominal stress. The stress concentration of the butt-welded specimen is mainly blamed on the existence of misalignment and the weld bead. Berge and Myhre [15] proposed a method to calculate the *SCF* due to axial misalignment [15]. By employing explainable machine learning, Braun et al. [16] found that macro-geometric axial and angular misalignment was the most influential parameter on the failure location of small-scale butt-welded joints. Chen et al. [17] reported that the failure location of butt joints with backing plates in fatigue tests could be accurately predicted with the traction structural stress method with considerations of angular joint misalignments. Qiu et al. [18] indicated that the plate thickness greatly influenced the fatigue reliability index of typical welded joints. The effect of the location of the weld and aspect ratio on the *SCF* was studied by Cui et al. [19].

However, for the specimen used in this study, the weld position is in the middle, so both the weld position and the aspect ratio have a negligible effect on the *SCF* calculation. Xing and Dong [14] found that the load-carrying fillet-welded specimens would deform during the grip-clamping process, which also affects the *SCF*. This study suggests that specimen deformation should also be considered when predicting the *SCF* of butt-welded specimens. In the meantime, the above-summarized *SCF* prediction methods for butt welds are the methods applied to structures, which cannot be directly applied to specimens because they do not consider the effect of the reduced section in the middle of the specimen on the hot-spot stress. In this study, the effect of the reduced midsection of the specimen on the stress concentration is taken into account and compared with the constant width model.

Meanwhile, these studies did not consider the effect of the bead on the *SCF*, so these methods are insufficient in predicting the *SCF*. The stress concentration caused by the weld

bead could be estimated using finite element analysis from a misalignment-free model, as reported by Kang et al. [20]. Lillemäe et al. [21] obtained the *SCF* by building a finite element model in which both the bead and misalignment were present. They indicated that the relationship between the hot-spot stress and the nominal stress is highly non-linear for the thin specimen. However, when multiple specimens with different misalignments need to be studied, the FE model needs to be re-established, resulting in lower efficiency. By introducing one additional stress concentration factor, Dong et al. [11] studied the effect of the weld bead on stress concentration. Instead, this study argues that the specimen experiences both axial and bending stresses during the experiment. So the effect of the bead on axial stress and bending stress should be considered separately. Finite element analysis is employed to individually investigate the stress concentrations caused by the bead on the tensile and bending specimens.

This study enhances existing methods by considering the combined effects of misalignment, bead, clamped grips, and reduced middle sections. The effect of the bead on axial and bending stresses is also studied separately. A comparison of this study with previous works is presented in Table 1. The prediction method is more suitable for predicting the hot-spot stress and the *SCF* of butt-welded specimens. To verify the feasibility of the proposed method, the predicted *SCF* is compared with the measured *SCF*. The results show that the experimentally obtained *SCF* is in good agreement with the predicted *SCF*. By using the method proposed in this study, it is possible to solve the disadvantages that may occur during strain measurement, such as incorrect installation and strain gauge detachment. It can also be used to check the validity of the *SCF* values obtained from the test if the actual test results deviate too much from expectations.

Table 1. Comparison of previous works and present study.

Author	Year	Bead Effect		Misalignment Effect				
		Axial Load	Bending Component	Axial Misalignment	Angular Distortion	Misalignment Location	Clamping Effect	Reduced Middle Section
Berge and Myhre adapted from Ref. [15]	1977	-	-	☑	☑	-	-	-
Cui et al. adapted from Ref. [19]	1999		-	☑	-	☑	-	-
Lillemäe et al. adapted from Ref. [21]	2012	☑	-	☑	☑	-	-	-
Kang et al. adapted from Ref. [20]	2015	☑	-	☑	☑	-	☑	-
Xing and Dong adapted from Ref. [14]	2016	-	-	☑	☑	☑	☑	-
Present study		☑	☑	☑	☑	☑	☑	☑

In the case of fillet specimens, Mashiri et al. [22] showed the differences in stress concentrations that occur from the different weld shapes. Hong et al. [23] used the peridynamic to simulate the fatigue process in a fillet weld. Chen et al. [24] investigated the fatigue performance of full-size fillet-welded specimens with incomplete penetration and misalignment of the weld root based on experimental tests and finite element analysis. A unified master S-N curve covering different plate thicknesses, materials, and weld profiles was also proposed [24]. The fatigue failure mode transition behavior of aluminum fillet-welded connections was analyzed systematically by Xing et al. [25]. Ahola and Björk [26] investigated the effect of specimen attachment misalignment on stress concentration and calculated the *SCF* using finite element analysis. Meanwhile, the effective notch stress

method and 4R method could be used in fillet-welded joint fatigue [27]. However, a method to predict the *SCF* by considering multiple weld dimensions does not exist yet. Meanwhile, measuring the profile with the 3D scanner would be laborious and could induce errors. Therefore, using the strain gauge to measure the hot-spot strain is more efficient for the fillet specimen.

The 2-wire strain gauge is commonly used at room temperature. However, using the 2-wire strain gauge directly in a cryogenic environment will reduce the accuracy of the experimental results. At cryogenic temperature, the 3-wire strain gauge is frequently used, but the cost of the experiment will increase. This study compares the output differences of the two strain gauges in the cryogenic environment. Based on the comparison results, a method of correcting the values obtained from the 2-wire strain gauge is proposed. The hot-spot stress of the fillet specimen can be measured more economically using the proposed calibration method.

In the present study, fatigue tests are conducted on three types of specimens: butt-welded, fillet longitudinal, and fillet transverse specimens at both room and cryogenic temperatures. The main objectives of this study are as follows: (1) to compare the fatigue characteristics of the three welded specimens at different temperatures and summarize the crack initiation position; (2) to optimize the method of studying the effect of misalignment on stress concentration; (3) to investigate the effect of the bead on stress concentration in specimens; and (4) to propose a strain gauge calibration method for cryogenic temperature testing.

2. Butt-Welded Specimens' *SCF* Prediction

2.1. Orientation and Measurement

Butt welding is a common connection in welded structures. There are four weld roots near the welding part. The welding direction of the specimen can be distinguished by checking the stacking sequence of the fish-scale-like pattern on the welded part. As shown in Figure 1a, the earlier welded part is on the lower layer, and the subsequent welded part is on the upper layer. Then, the front and back of the specimen can be distinguished according to the size of the bead, as shown in Figure 1b. The base material (BM), heat-affected zone (HAZ), and weld metal (WM) in the specimen have been marked in Figure 1b. In this way, the orientation of each specimen can be defined, where w is the width of the specimen, and t is the thickness of the specimen.

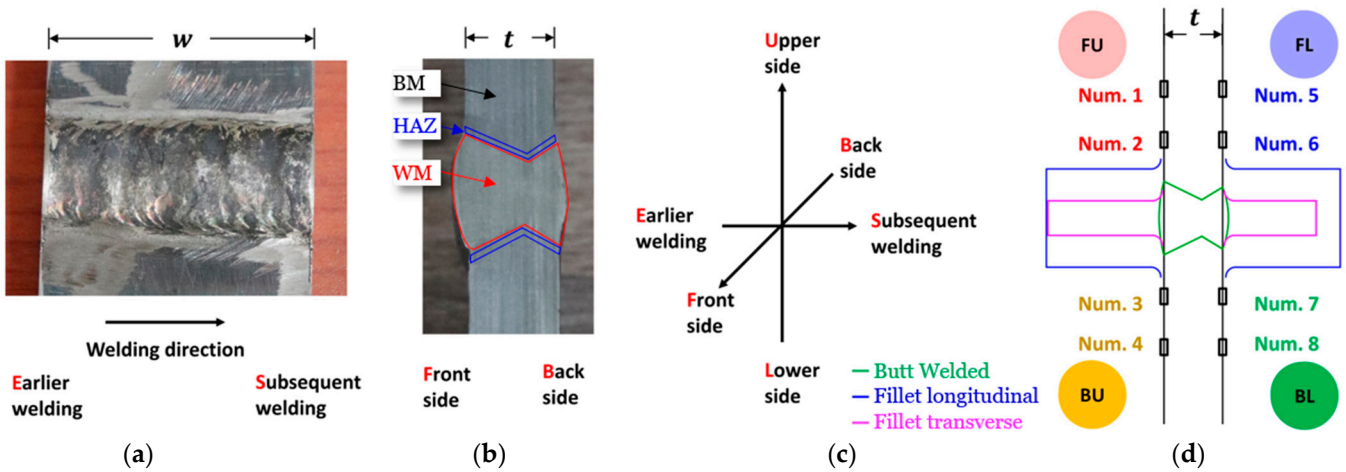
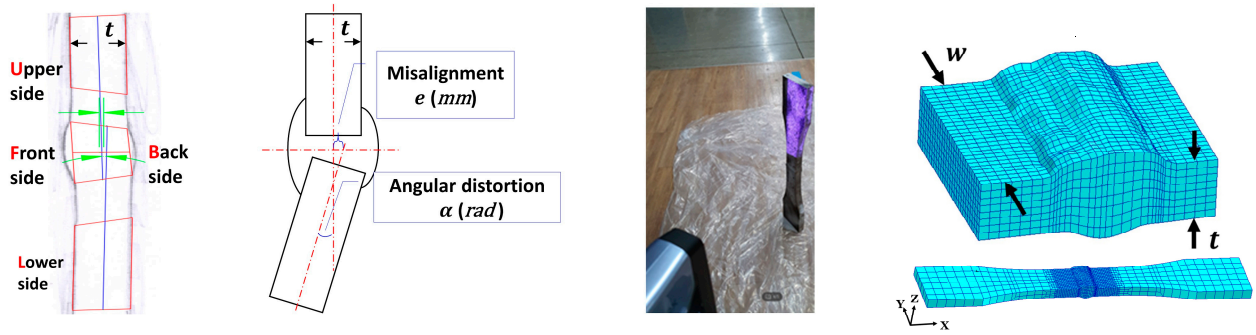


Figure 1. Butt-welded specimens' orientation. (**a**) E and S distinction; (**b**) F and B distinction and specific areas for the materials; (**c**) total orientation; (**d**) gauge and hot-spot naming.

For a better understanding, E (Earlier welding), S (Subsequent welding), F (Front), B (Back), U (Upper), and L (Lower) are employed, as shown in Figure 1c. Furthermore, the weld root could be named using FU, FL, BU, and BL corresponding to the position

shown in Figure 1d. Eight strain gauges are installed on both sides of the specimen to measure the strain, and the numbers from 1 to 8 denote the eight strain gauges, respectively, as shown in Figure 1d. The specimen thickness (t) is 12 mm. By measuring the strain at 0.5t (6 mm) and 1.5t (18 mm) from the weld root, the hot-spot strain can be obtained by the linear extension method.

The profiles on both sides of each specimen are measured to study the misalignment effect. The average value on both sides is taken as the misalignment of the specimen. Importing the profiles into AutoCAD for measurement is shown in Figure 2a. Since the specimen direction has already been distinguished, the direction of the axial misalignment and angular distortion can be defined, as shown in Figure 2b. The bead appearance is obtained by 3D scanning, as shown in Figure 2c and translated to the FE model for further analysis, as presented in Figure 2d.



(**a**) (**b**) (**c**) (**d**)

Figure 2. Misalignments and bead measurement. (**a**) Measuring the misalignment; (**b**) misalignments direction definition; (**c**) scanning the bead; (**d**) establishing the finite element model.

2.2. SCF Prediction Method Review

The *SCF* is the ratio between the hot-spot stress (σ_{hs}) and nominal stress (σ_{nom}), as in Equation (1):

$$SCF = \sigma_{hs}/\sigma_{nom} \quad (1)$$

The classical *SCF* calculation method considers the effects due to the specimen's initial axial misalignment (e) and angular distortion (α), and the analytical equations are applied based on the simple beam theory as in Equation (2) [15].

$$SCF = 1 + \lambda e/t + \lambda \alpha L/4t = 1 + k_{mis} + k_{ang} \quad (2)$$

where the following apply:

k_{mis}: the stress magnification factor due to axial misalignment (dimensionless);
k_{ang}: the stress magnification factor due to angular distortion (dimensionless);
λ: 3 for clamped; 6 for pinned condition;
L: the total length of the specimen (mm);
t: the thickness of the specimen (mm).

As for standards, like BS 7910 [28], IIW [29], and DNV [30], they consider the nominal stress effect. However, this effect is negligible for the specimens which are tested in this study. DNV also considers misalignment tolerance, $e_{cal} = e - 0.1t$. The misalignment used to calculate (e_{cal}) is the actual misalignment (e) minus 0.1t.

2.3. Stress Components

Due to misalignment, bending stress is induced in the specimen during the gripping procedure before the fatigue test. At this moment, though the nominal stress (σ_{nom}) is zero, the hot-spot stress is non-zero. So in the subsequent fatigue experiments, the total hot-spot

stress (σ_{hs}) has two components: (1) hot-spot stress initiated by gripping ($\sigma_{hs,grip}$) and (2) hot-spot stress initiated by nominal stress ($\sigma_{hs,nom}$), as in Equation (3).

$$SCF = \sigma_{hs}/\sigma_{nom} = \left(\sigma_{hs,nom} + \sigma_{hs,grip}\right)/\sigma_{nom} \tag{3}$$

In the fatigue test, the loading amplitude is valuable to study, defining the SCF_{Δ} as in Equation (4). The σ_{max} and σ_{min} correspond to the maximum and minimum values during the loading process.

$$SCF_{\Delta} = (\sigma_{hs,max} - \sigma_{hs,min})/(\sigma_{nom,max} - \sigma_{nom,min}) = \sigma_{hs,nom}/\sigma_{nom} \tag{4}$$

Combine Equations (3) and (4), and the relationship between σ_{hs} and σ_{nom} is given by Equation (5).

$$\sigma_{hs} = \sigma_{hs,nom} + \sigma_{hs,grip} = SCF_{\Delta} \times \sigma_{nom} + \sigma_{hs,grip} \tag{5}$$

As shown in Figure 3, the slope represents SCF_{Δ}, while the intercept represents $\sigma_{hs,grip}$.

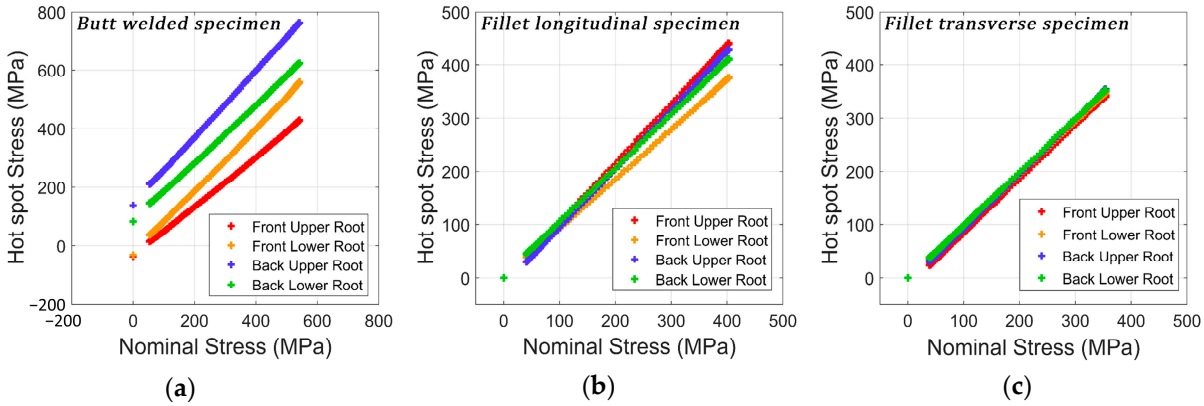


Figure 3. Relationship between nominal stress and hot-spot stress. (**a**) Butt-welded specimen; (**b**) fillet longitudinal specimen; (**c**) fillet transverse specimen.

Shen et al. [31] stated that the stress magnification factor could decrease as the nominal stress increases. However, Figure 3a shows that the slope of the $\sigma_{nom} - \sigma_{hot}$ curve is invariant. In this way, the SCF_{Δ} of the specimen in this study is not a function of σ_{nom}. During the fatigue test, the specimen is subjected to periodic tensile load, and its stress distribution can be divided into two parts: axial nominal stress and bending stress. By adopting the superposition principle, the bending stresses due to axial misalignment and angular distortion could be discussed separately. For instance, the stress distribution can be presented in Figure 4 when considering the axial misalignment. The k_{mis} represents the stress magnification factor due to axial misalignment.

The total stress has two components: (a) nominal stress for balancing the axial load ($\Delta\sigma_{axial}$); and (b) bending stress for balancing the moment due to misalignment ($\Delta\sigma_{bend,mis}$). The axial nominal stress remains constant in the thickness direction, but the bending stress varies linearly through the thickness and becomes zero at the neutral line. The axial nominal stress is equal to the load applied to the specimen. The bending stress is proportional to the nominal stress and also depends on the magnitude of misalignment.

Thus, the total stress could be written as in Equation (6).

$$\Delta\sigma_{axial} + \Delta\sigma_{bend,mis} = \Delta\sigma_{nom} + \Delta\sigma_{nom} \times k_{mis} = \Delta\sigma_{nom}(1 + k_{mis}) \tag{6}$$

Considering the angular distortion existing case, the stress could be written as in Equation (7). The k_{ang} is the stress magnification factor due to angular distortion.

$$\Delta\sigma_{axial} + \Delta\sigma_{bend,ang} = \Delta\sigma_{nom} + \Delta\sigma_{nom} \times k_{ang} = \Delta\sigma_{nom}\left(1 + k_{ang}\right) \tag{7}$$

When both axial misalignment and angular distortion exist, using the principle of superposition, Equation (8) can be obtained:

$$\Delta\sigma_{hs} = \Delta\sigma_{axial} + \Delta\sigma_{bend,mis} + \Delta\sigma_{bend,ang} = \Delta\sigma_{nom}\left(1 + k_{mis} + k_{ang}\right) \quad (8)$$

The first term represents axial nominal stress, while the second and the third term represent bending stress due to the misalignment. The magnitude of the k_{mis} or k_{ang} should be the same for different roots. However, the direction of the bending stress is opposite on both sides. Table 2 gives the sign of the stress for each root, where "+" indicates tension and "−" indicates compression.

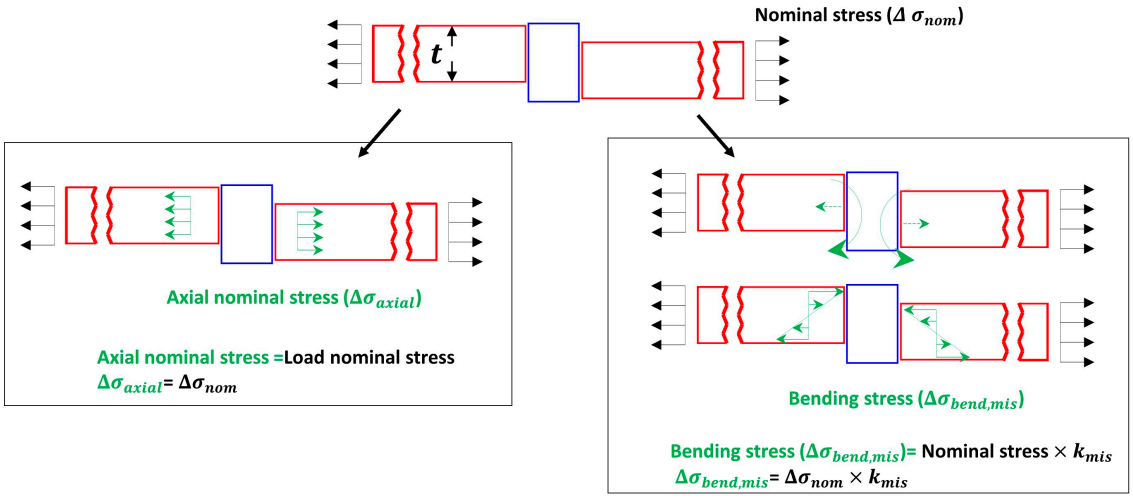


Figure 4. Stress distribution in axial misalignment model.

Table 2. Stress direction at four roots.

Root Position	Front Upper	Front Lower	Back Upper	Back Lower
Sign (k_{mis})	−	+	+	−
Sign (k_{ang})	+	+	−	−

2.4. The Bead Effect

At the welding position, the weld bead is present. Unlike the base material specimen, this results in an inhomogeneous stress distribution, regardless of whether the specimen is subjected to axial tension or bending load. In order to study the impact of the bead, k_{bead} is employed. The k_{bead} is defined as the ratio of hot-spot stress to nominal stress when the specimen with a bead receives tensile stress or bending stress. Also, this study suggests that the effect of beads on axial tensile stress ($k_{bead,axial}$) and bending stresses ($k_{bead,bend}$) should be considered separately.

This part focuses exclusively on the effect of the bead. Therefore, the FE model is constructed without incorporating axial misalignment or angular distortion. Although each specimen has a unique contour at the bead part, scanning is laborious, and there is minimal variation between specimens. Consequently, only one specimen's contour is scanned, and the finite element model is based on these scanning results.

The model is created using Patran 2011, and the finite element analysis is conducted using MSC-Nastran 2011. The entire specimen utilizes 8-node Hex8 elements with a minimum mesh size of 1 mm. Larger mesh sizes are used in the clamped portion of the specimen at both ends, which improves the simulation efficiency, while smaller mesh sizes are used in the bead region of the model. The mesh details are illustrated in Figure 5. The mesh division method is referenced from Kang's study [20].

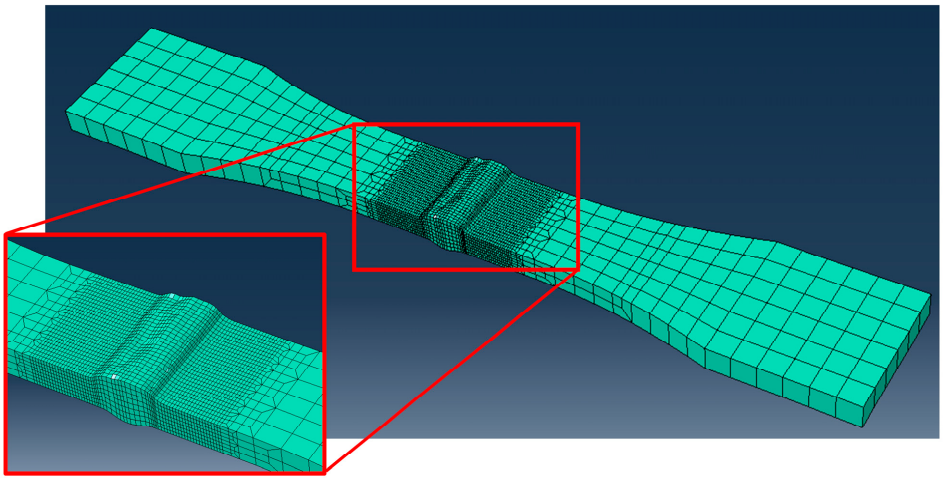
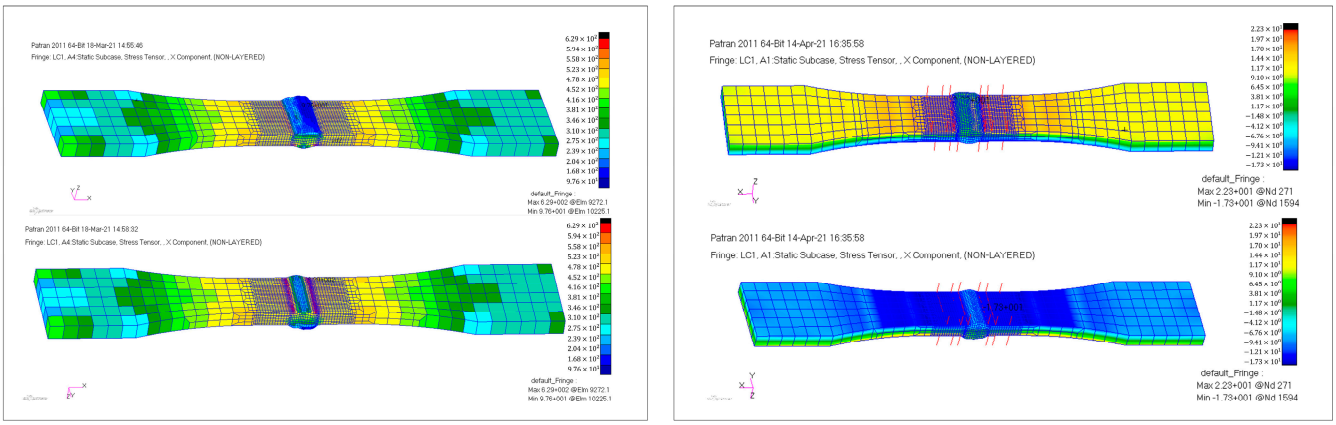


Figure 5. The model of the butt specimen.

The elastic modulus of 9% Ni steel is set to 196.3 MPa, and Poisson's ratio is set as 0.3. For the boundary conditions, the nodes on one side are fixed. With reference to Kang's study [20], apply the axial tensile stress ($\sigma_{nom,axial,FE}$) or bending stress ($\sigma_{nom,bend,FE}$) on the other side as the loading condition. The results are shown in Figure 6.



(**a**) (**b**)

Figure 6. The FE results for studying the bead effect. (**a**) Tensile load applied case; (**b**) bending load applied case.

Selecting the stress located at 0.5t (t, thickness) and 1.5t from the weld bead, the hot-spot stress ($\sigma_{hs,axial,FE}$ or $\sigma_{hs,bend,FE}$) could be calculated using linear extrapolation. The bead effect parameter for the tensile load case ($k_{axial,FE}$) and bending load case ($k_{bend,FE}$) can be obtained by computing the ratio of the hot-spot stress to the nominal stress, as presented in Equations (9) and (10):

$$k_{axial,FE} = \sigma_{hs,axial,FE} / \sigma_{nom,axial,FE} \quad (9)$$

$$k_{bend,FE} = \sigma_{hs,bend,FE} / \sigma_{nom,bend,FE} \quad (10)$$

2.5. The Clamped and Reduced Mid-Section Effect

Since the specimen is not flat, when the grip is clamped, not only will the bending stress (σ_{grip}) appear, but the specimen will also deform, which would affect the subsequent fatigue tests [14]. The so-called clamped effect refers to the influence of this deformation, as shown in Figure 7.

Due to the lack of considering the influence of the clamped effect, the classical k_{mis} and k_{ang} calculation methods are insufficient. In reference [14], the authors introduced a method for predicting the SCF_{Δ} that takes into account the clamped effect in load-carrying fillet specimens, as shown in Figure 8a.

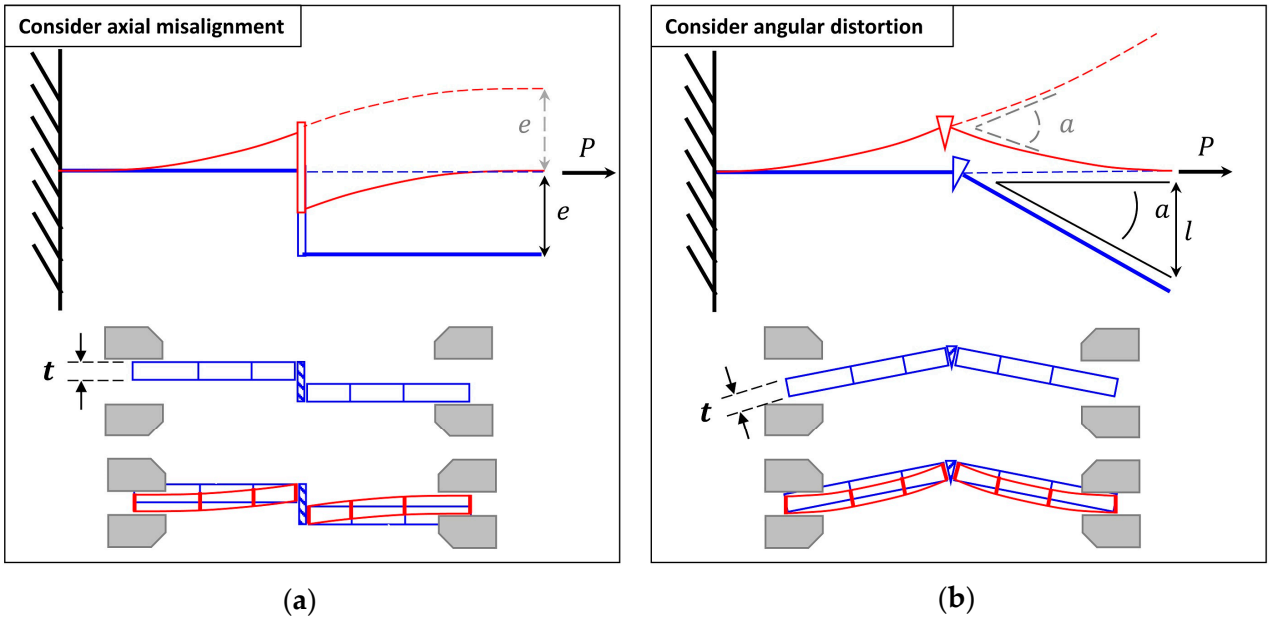


Figure 7. Deformation of the specimen after grips are clamped. (**a**) Axial misalignment case; (**b**) angular distortion case. (Blue lines: before deformation, red lines: after deformation).

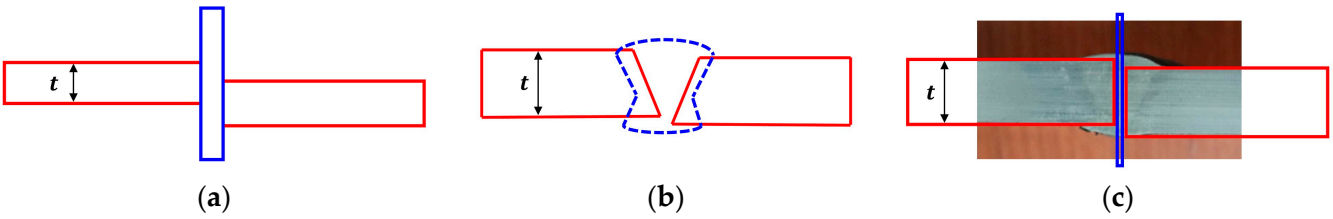


Figure 8. Schematic view of the specimens (simplified figures). (**a**) The load-carrying fillet specimen; (**b**) the butt specimen before welding; (**c**) translating the butt specimen into three parts (Red lines: base metal, blue lines: weld zone).

The butt-welded specimen is welded by two base materials; adding the welding part in the middle, the specimen can be divided into three parts, as shown in Figure 8b. Although the bead sizes on both sides of the specimen are different (16 mm and 18 mm), the difference is narrow and could be ignored. Assuming the welded portion forms a thin rectangle, the butt-welded specimen would exhibit a configuration similar to that of the load-bearing fillet specimen, as shown in Figure 8c. In this way, it is found that the model predicting the fillet specimen's SCF_{Δ} can also be used for butt-welded specimens.

The specimen used in this study has a narrow width in the middle section. The narrow mid-section is widely used in experimental studies, and the reduced mid-section is also recommended in the ASTM standard E466 [32]. The narrow middle section ensures that failure occurs at the welded part during the experiment. Therefore, the reduction in the mid-section should be taken into account.

Therefore, this study improves this model and finds that considering or not considering the reduction in the mid-section has a non-negligible effect on the SCF_{Δ} prediction. In the reference, the model is only divided into left and right parts, as shown in Figure 9a. To consider the impact of the reduced mid-section, we divided the specimen into six parts,

which have different widths, as w_1, w_2, w_3, …, w_6, as shown in Figure 9, and $L_1 = 5$mm, $L_2 = 85$m, $L_3 = 45$mm in Figure 9b.

For example, for the Num. 1 specimen, the comparison between the specimen with considering or without considering the narrow mid-section after clamping the specimen is shown in Figure 10.

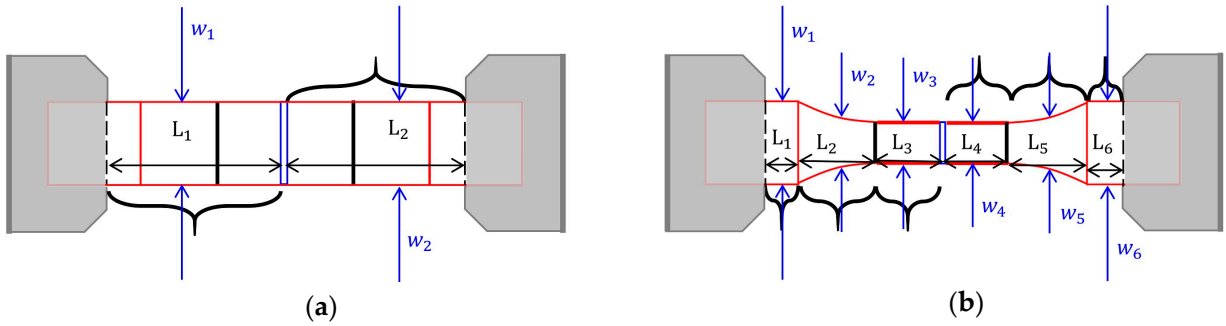


Figure 9. Dividing the specimen into several parts according to the width. (**a**) Two parts; (**b**) six parts.

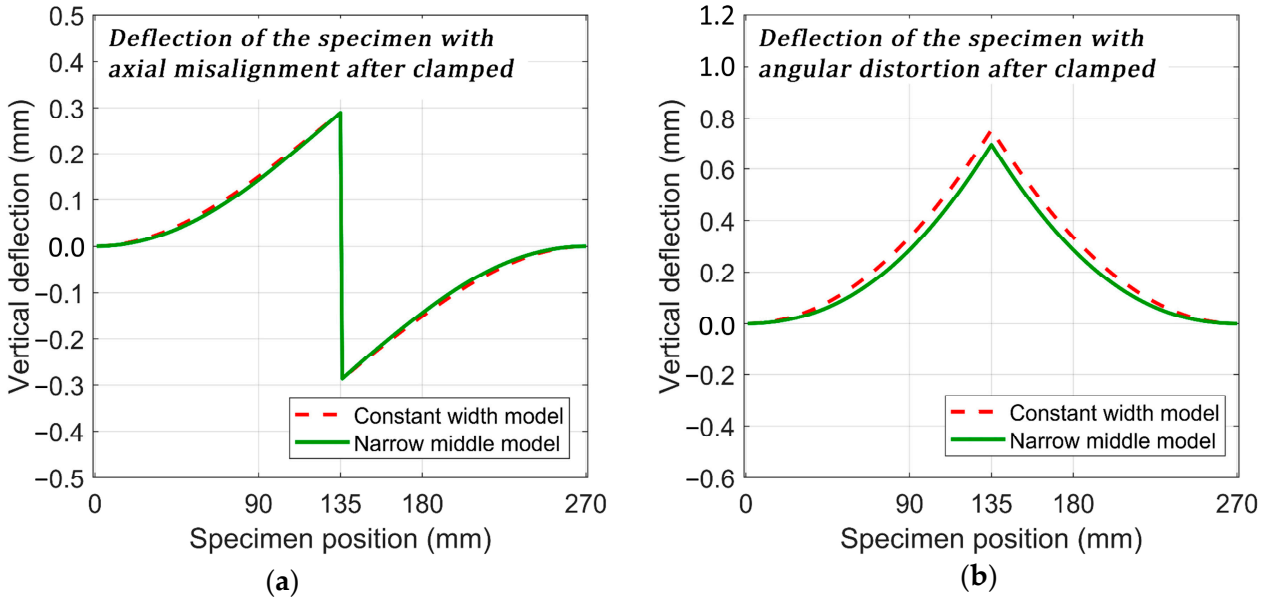


Figure 10. The specimen deflection after grips are clamped (**a**) Axial misalignment case; (**b**) angular distortion case.

By using the method reported in the reference [14], the bending stress due to the axial misalignment ($\Delta\sigma_{bend,mis}$) and angular distortion ($\Delta\sigma_{bend,ang}$) could be calculated. Then the k_{mis} and k_{ang} are given by Equations (11) and (12).

$$k_{mis} = \Delta\sigma_{bend,mis} / \Delta\sigma_{nom} \tag{11}$$

$$k_{ang} = \Delta\sigma_{bend,ang} / \Delta\sigma_{nom} \tag{12}$$

The k_{mis} and k_{ang} of the Num. 1 specimen are given in Figure 11.

By considering the effect of the bead on axial nominal stress and bending stress separately, the SCF_Δ for the butt specimen could be obtained as in Equation (13).

$$\begin{aligned} SCF_\Delta = \frac{\Delta\sigma_{hs}}{\Delta\sigma_{nom}} &= \left[k_{bead,axial} \times \Delta\sigma_{nom} + k_{bead,bend} \times \left(\left(k_{mis} + k_{ang}\right) \times \Delta\sigma_{nom}\right)\right] / \Delta\sigma_{nom} \\ &= k_{bead,axial} + k_{bead,bend} \times \left(k_{mis} + k_{ang}\right) \end{aligned} \tag{13}$$

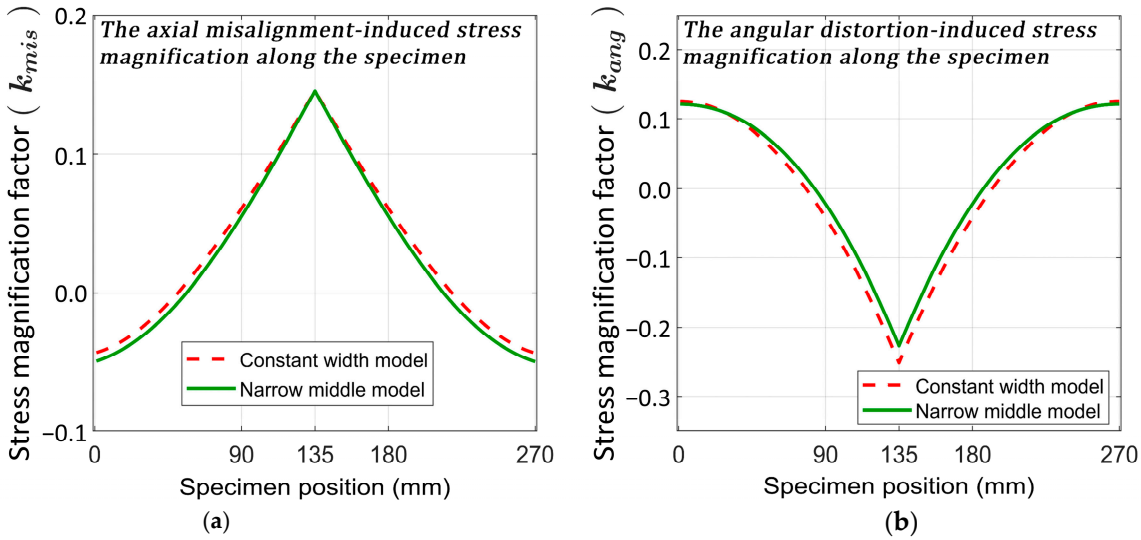


Figure 11. The misalignment-induced stress magnification along the specimen. (**a**) Axial misalignment case; (**b**) angular distortion case.

3. Calibrating the 2-Wire Strain Gauge Output

For cryogenic temperature tests, the accuracy of the general 2-wire strain gauge could be reduced. Therefore, the cryogenic 3-wire strain gauge should be employed to maintain accuracy. As a consequence, the cost would increase. A correcting method is introduced in this section to improve the accuracy of the 2-wire strain gauge in a cryogenic environment.

The strain measurement system has two components: strain gauge and data acquisition system (DAQ) devices. The strain gauge can investigate the attached object deformed by measuring the resistance change. After the gauge is deformed, the strain (ε) could be obtained, given in Equation (14), where R_G is the gauge resistance (Ω), and K is the gauge factor at the corresponding temperature.

$$\varepsilon = (\Delta R_G / R_G)/K \tag{14}$$

The gauge resistance and gauge factor are supplied by the gauge manufacturer. The circuit diagram in the DAQ device is shown in Figure 12a. Any change in resistance R_G can be reflected as a change in V_0, given in Equation (15), where R_1, R_2, R_3, and V_{EX} are fixed values in the DAQ device.

$$V_0 = [R_3/(R_3 + R_G) - R_2/(R_1 + R_2)] \times V_{EX} \tag{15}$$

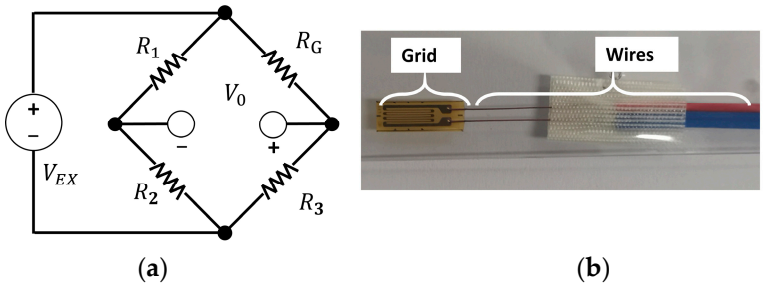


Figure 12. The strain investigating system introduction. (**a**) Wheatstone bridge circuit diagram in DAQ; (**b**) strain gauge.

The strain gauge can be divided into two parts, which are the grid of the gauge and the wires of the gauge, as shown in Figure 12b. Both the grid and the wires have resistance,

which are R_{Gr}, R_W. In fact, when experimenting in a fixed-temperature environment, R_W is a constant value. So the gauge resistance change ΔR_G is equivalent to the gauge grid resistance change ΔR_{Gr}. The circuit diagrams of the 2-wire strain gauge and the 3-wire strain gauge are illustrated in Figure 13.

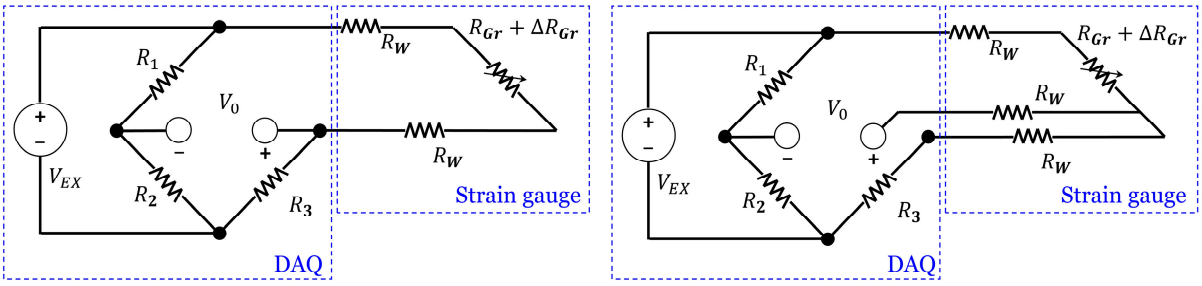


Figure 13. The strain gauge circuit connection diagram. (**a**) The 2-wire strain gauge case; (**b**) the 3-wire strain gauge case.

The wires are made of copper, so the resistance is sensitive to temperature changes. If the experiment is executed at varying temperatures, the resistance of the wire (R_W) will change with the temperature. The resistance change in the wires will affect the accuracy of measuring the resistance change due to gauge grid deformation (ΔR_{Gr}). Therefore, the strain of the attached object cannot be measured correctly. As for the 3-wire strain gauge, as shown in Figure 13b, the resistance of the wire $R_{W,1}$ is in a series with the gauge grid and the resistance of the wire R_W is in a series with the R_3. Since equal resistance changes which occur simultaneously in the adjacent arms of a bridge circuit produce no bridge imbalance, temperature changes which affect R_W together are effectively cancelled [33]. This is the temperature compensation for the 3-wire strain gauge.

For fixed-temperature cryogenic experiments, the 3-wire strain gauge can be used directly since the manufacturer provides the value of the gauge factor under the cryogenic temperature ($K_{3w,cryo.}$). The strain measured at cryogenic temperature by the 3-wire strain gauge is $\varepsilon_{3w,cryo}$, given in Equation (16). $R_{3w,Gr}$ is the 3-wire strain gauge grid resistance.

$$\varepsilon_{3w,cryo} = \Delta R_{3w,Gr} / \left(R_{3w,Gr} \times K_{3w,cryo.} \right) \tag{16}$$

For the 2-wire strain gauge, when the experiment is carried out in a constant-temperature cryogenic environment, the R_W would change during the cooling process from normal temperature to low temperature. However, in the subsequent experiments, R_W is a constant value since the temperature is fixed. The value used to calculate the strain is the change in resistance during the test, so changes in R_W during the cooling process will not affect subsequent test results measurement. The accurate strain ($\varepsilon_{2w,cryo,ac}$) could be obtained by Equation (17). $K_{2w,cryo}$ is the 2-wire strain gauge's gauge factor at cryogenic temperature and $R_{2w,Gr}$ is 2-wire strain gauge grid resistance.

$$\varepsilon_{2w,cryo,ac} = \Delta R_{2w,Gr} / \left(R_{2w,Gr} \times K_{2w,cryo} \right) \tag{17}$$

However, since the 2-wire strain gauge is not designed for cryogenic temperature experiments, the gauge factor ($K_{2w,cryo}$) at cryogenic temperature may not be provided by the manufacturer. Directly using the gauge factor of 2-wire strain gauges at room temperature ($K_{2w,room}$) as in Equation (18) would make the strain result ($\varepsilon_{2w,cryo,inac}$) inaccurate.

$$\varepsilon_{2w,cryo,inac} = \Delta R_{2w,Gr} / \left(R_{2w,Gr} \times K_{2w,room} \right) \tag{18}$$

Theoretically, under the same loading condition, if the correct gauge factor ($K_{2w,cryo}$) is used, the strain measured by the 2-wire strain gauge ($\varepsilon_{2w,cryo,ac}$) and the strain measured by the 3-wire strain gauge ($\varepsilon_{3w,cryo}$) should be the same, as summarized in Equation (19).

$$\varepsilon_{3w,cryo} = \Delta R_{3w,Gr} / \left(R_{3w,Gr} \times K_{3w,cryo} \right) = \varepsilon_{2w,cryo,ac} = \Delta R_{2w,Gr} / \left(R_{2w,Gr} \times K_{2w,cryo} \right) \quad (19)$$

By simplifying Equations (17)–(19), Equation (20) can be obtained as follows:

$$\varepsilon_{2w,cryo,ac} / \varepsilon_{2w,cryo,inac} = \varepsilon_{3w,cryo} / \varepsilon_{2w,cryo,inac} = K_{2w,room} / K_{2w,cryo} \quad (20)$$

where $\varepsilon_{2w,cryo,ac} / \varepsilon_{2w,cryo,inac}$ represents the ratio of the inaccurate strain to the correct strain. It can be seen that the invariant $\varepsilon_{2w,cryo,ac} / \varepsilon_{2w,cryo,inac}$ is not a function of $\Delta R_{2w,Gr}$ or $\Delta R_{3w,Gr}$, indicating that this value is not affected by the elongation of the specimen. It means that this value is invariable under different stress conditions.

To obtain this value, the plate specimen is made as shown in Figure 14. The specimen was designed with reference to ASTM E8/E8M [34]. The 2-wire strain gauge and the 3-wire strain gauge are attached to the specimen. By stretching the specimen, strain gauges will show different outputs at cryogenic temperatures as $\varepsilon_{3w,cryo}$ and $\varepsilon_{2w,cryo,inac}$. At the same time, a comparative experiment is performed at room temperature. The strain measured at room temperature by the 3-wire strain gauge is $\varepsilon_{3w,room}$ and the strain measured by the 2-wire strain gauge is $\varepsilon_{2w,room}$.

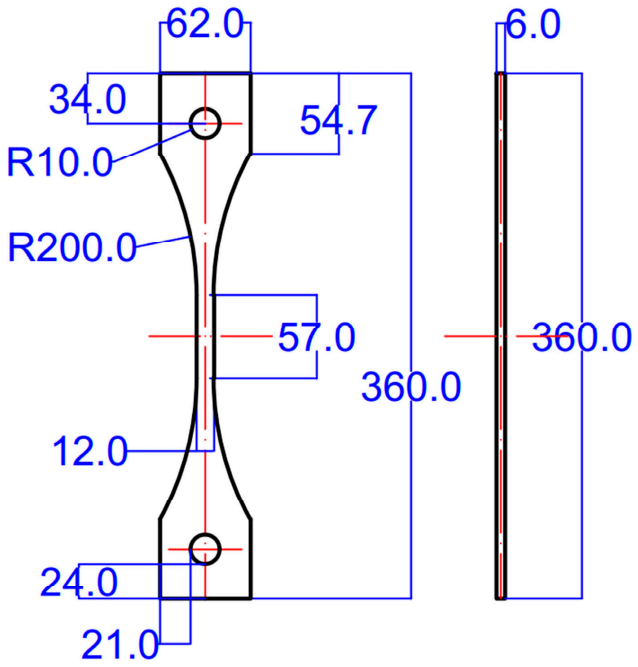


Figure 14. Plate specimen dimensions (unit: mm).

It can be seen from Figure 15 that at room temperature, $\varepsilon_{3w,room} / \varepsilon_{2w,room} = 1$. It indicates that under room temperature, the outputs from the different gauges are the same. However, at cryogenic temperature, the output of the 2-wire strain gauge is smaller, and $\varepsilon_{3w,cryo} / \varepsilon_{2w,cryo,inac}$ is a stress-independent constant value which is 1.048. Through Equation (20), it can be seen that the $\varepsilon_{2w,cryo,ac} / \varepsilon_{2w,cryo,inac}$ is 1.048. Then, the inaccurate output measured by the 2-wire strain gauge at cryogenic temperatures can be corrected by using this value. In this way, the 2-wire strain gauge can be used more accurately for cryogenic experiments.

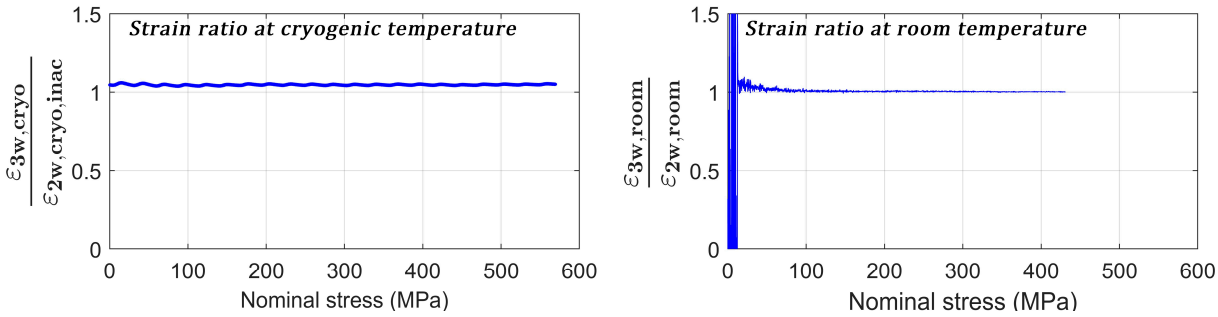


Figure 15. The ratio between strain measured by 3-wire gauge and strain measured by 2-wire gauge. (**a**) At cryogenic temperature; (**b**) at room temperature.

4. Fatigue Test and Test Results

4.1. Test Introduction

Three kinds of specimens are tested, including the butt-welded, fillet transverse, and fillet longitudinal specimens. The 9% Ni steel is supplied by POSCO located in Pohang, Republic of Korea. The material properties are given in Appendix A. The universal testing machine and its operating system are provided by MTS, with a maximum load capacity of ±50 tons. The cryogenic test chamber is manufactured by R&B with an operating temperature range of −180 to 80 °C. The apparatus is shown in Figure 16. The calibration of the machines was conducted within the six months prior to the test.



(**a**) (**b**)

Figure 16. The universal testing machine with cryogenic test chamber. (**a**) MTS ± 10 tons grips and controllers; (**b**) MTS ± 50 tons grips and R&B chamber (Source: ost.snu.ac.kr).

The tests are carried out at room (20 °C) and cryogenic (163 °C) temperatures. The specimen dimensions and the welding information are shown in Figure 17 and Table 3, respectively. The specimens are welded using flux-cored arc welding (FCAW). For the butt-welded specimens, 1G welding is employed, while the fillet-welded specimens use 2F welding, as shown in the following figures.

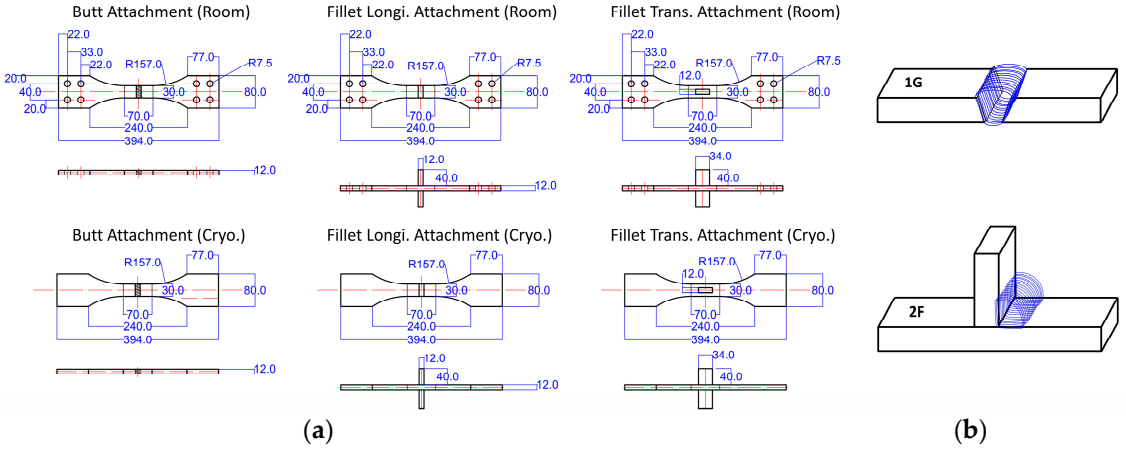


Figure 17. Fatigue test specimens' induction (unit: mm). (**a**) The specimen dimensions; (**b**) the welding position.

Table 3. Specimens' welding information.

Test Item	Welding Process	Thickness (mm)	Welding Position
Butt-Welded	FCAW	12	1G
Fillet Longitudinal	FCAW	12	2F
Fillet Transverse	FCAW	12	2F

The specimen design refers to the ASTM E466 [32]. The force ratio (r) is 0.1 (kN/kN), and the test frequency is 6 to 15 Hz. During the cryogenic temperature test, the specimens are kept in the chamber for 1.5 h before the experiment to allow the specimen to cool completely, and experiments are carried out without interruption. During the cryogenic temperature test, the temperature of the specimens is maintained within ±1 degree of the target temperature. For strain measurement, the data acquisition system (DAQ) devices are from National Instruments, and the strain gauges are from KYOWA. In the area where the strain gauge is installed, the specimen is first ground using an angle grinder, followed by polishing with sandpaper, and then wiped with acetone.

4.2. S-N Curve

To describe the relationship between stress amplitude ($\Delta\sigma$) and fatigue life (N), the S-N curve is employed as in Equation (21). The m and a are fatigue life curve parameters.

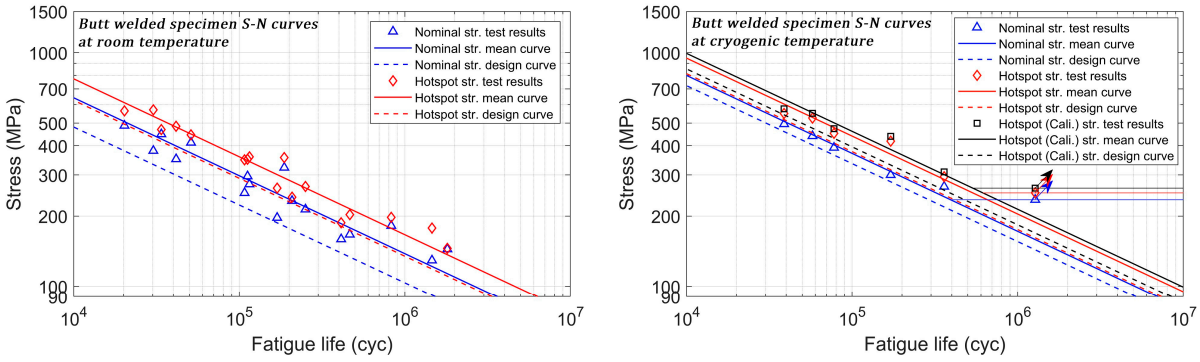
$$log\Delta\sigma = (-logN + loga)/m \tag{21}$$

The S-N design curve is determined with 97.7% of survivability, as shown in Equation (22), where STD is the standard deviation.

$$log\Delta\sigma = (-logN + loga - 2STD)/m \tag{22}$$

For the cryogenic temperature test, the corrected ratio $\varepsilon_{2w,cryo,ac}/\varepsilon_{2w,cryo,inac}$ is used to calibrate the results measured by the 2-wire strain gauge. The S-N curves of three specimens are illustrated in Figures 16–18. The S-N curve parameter is given in Table 4.

The FAT value refers to the corresponding stress on the curve when fatigue life $N = 2 \times 10^6$ (cycles) and this value can be called fatigue strength. FAT(M) stands for the mean curve, and FAT(M-2STD) stands for the design curve. Figures 18–20 also show that specimens at cryogenic temperature could provide higher fatigue resistance than at room temperature. Table 4 shows that the S-N curve based on nominal stress has a smaller correlation coefficient (r^2) than the S-N curve based on hot-spot stress.



(**a**) (**b**)

Figure 18. The butt-welded specimen test results and S-N curves. (**a**) Room temperature test; (**b**) cryogenic temperature test. (The arrow indicates that the fatigue limit is reached and the test is stopped manually).

Table 4. The S-N curve parameter.

Fatigue Test Results (*loga* Represents the Logarithm Based on *e*)			**Butt-Welded Specimen**	**Fillet Longitudinal Specimen**	**Fillet Transverse Specimen**
Room Temperature	$\Delta\sigma_{nom}$ –N Curve	*loga*	28.60	29.08	28.58
		r^2	0.8897	0.9841	0.9155
		FAT(*M*)	109.7	128.8	108.8
		FAT(*M*-2*STD*)	82.2	114.7	84.6
	$\Delta\sigma_{hs}$ –N Curve	*loga*	29.16	29.61	28.75
		r^2	0.9403	0.9600	0.9439
		FAT(*M*)	132.2	153.4	115.4
		FAT(*M*-2*STD*)	106.9	127.5	94.0
Cryogenic Temperature	$\Delta\sigma_{nom}$ –N Curve	*loga*	29.26	29.47	28.87
		r^2	0.9642	0.9132	0.942
		FAT(*M*)	136.7	146.4	120.0
		FAT(*M*-2*STD*)	123.6	118.2	104.9
	$\Delta\sigma_{hs}$ –N Curve	*loga*	29.77	29.68	29.01
		r^2	0.9174	0.9686	0.9841
		FAT(*M*)	162.0	157.4	125.8
		FAT(*M*-2*STD*)	139.0	138.4	117.3
	$\Delta\sigma_{hs,cali}$ –N Curve	*loga*	29.91	29.82	29.15
		r^2	0.9174	0.9686	0.9841
		FAT(*M*)	169.8	164.5	131.9
		FAT(*M*-2*STD*)	145.7	145.0	122.9

Note: a = fatigue life curve parameter, r^2= correlation coefficient, $\Delta\sigma_{nom}$ = nominal stress range, $\Delta\sigma_{hs}$ = hot-spot stress range, $\Delta\sigma_{hs,cali}$ = hot-spot stress range after calibration, N = fatigue life, *FAT*(*M*) = the corresponding stress on the mean curve when fatigue life $N = 2 \times 10^6$ (cycles), *FAT*(*M*-2*STD*) = the corresponding stress on the design curve when fatigue life $N = 2 \times 10^6$ (cycles).

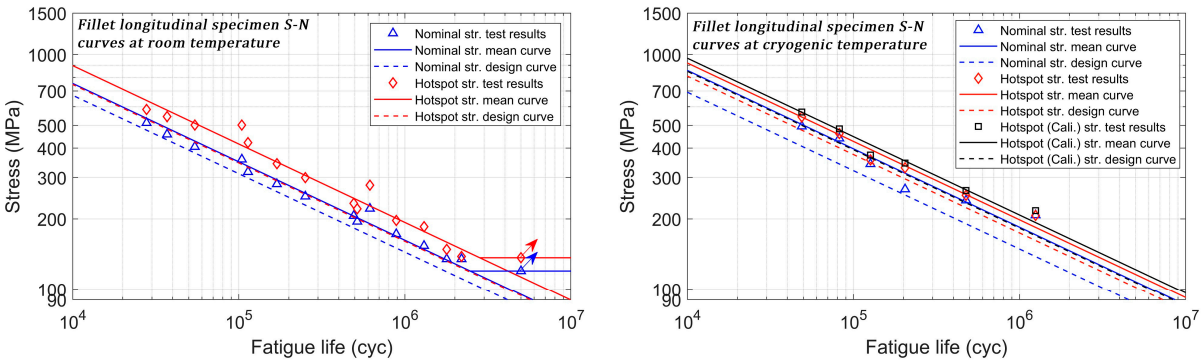


Figure 19. The fillet longitudinal specimen test results and S-N curves. (**a**) Room temperature test; (**b**) cryogenic temperature test (The arrow indicates that the fatigue limit is reached and the test is stopped manually).

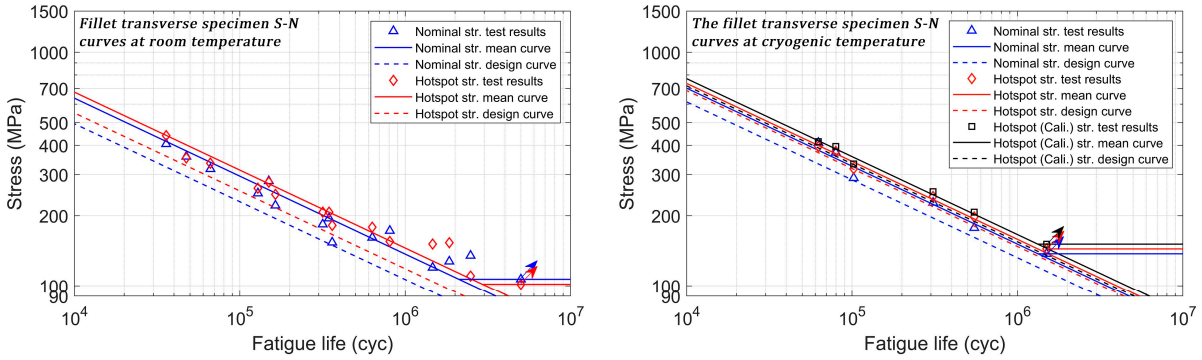


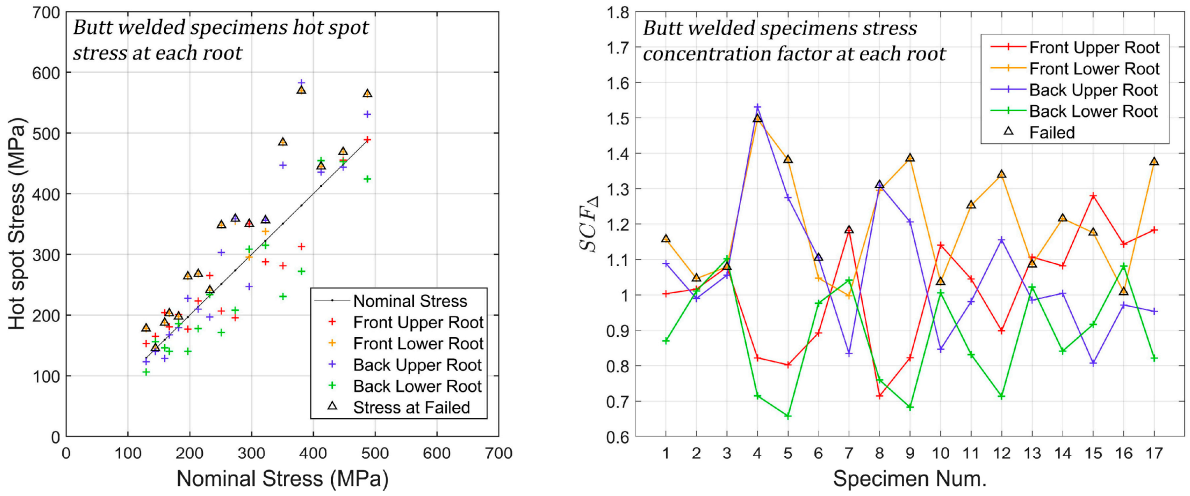
Figure 20. The fillet transverse specimen test results and S-N curves. (**a**) Room temperature test; (**b**) cryogenic temperature test (The arrow indicates that the fatigue limit is reached and the test is stopped manually).

4.3. Fracture Point

According to the direction of the specimen, the four hot spots could be named as "FU, FL, BU, BL". For the butt-welded specimens, as shown in Figure 21, most of the cracks tend to appear where the SCF_{Δ} is the largest.

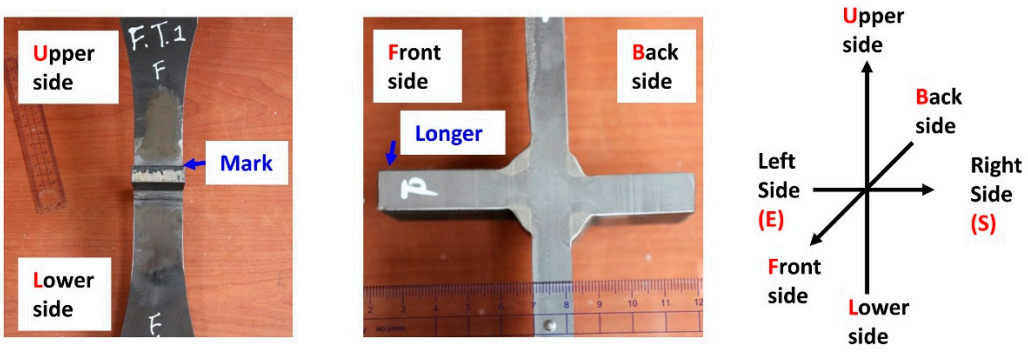
For the fillet longitudinal specimen, the orientation is set randomly because the specimen's orientation cannot be distinguished. For the fillet transverse specimen, the orientation of specimens can be distinguished according to the attachment, and the orientations of the fillet transverse specimens are shown in Figure 22.

It can be seen from Figures 23 and 24, which are for the fillet specimen, that the cracks do not appear where the hot-spot stress is the largest. Figure 3b,c show that the intercept of each curve is exceedingly small, indicating that in the process of grip closing, compared with the butt-welded specimen, only a tiny bending stress is generated in the fillet specimen. Therefore, the initial bending stress does not affect the location of crack generation. For some specimens, cracks could appear at the weld root where the SCF_{Δ} is less than 1.0. In addition to the SCF_{Δ}, the appearance of the weld root also affects the appearance of the crack.



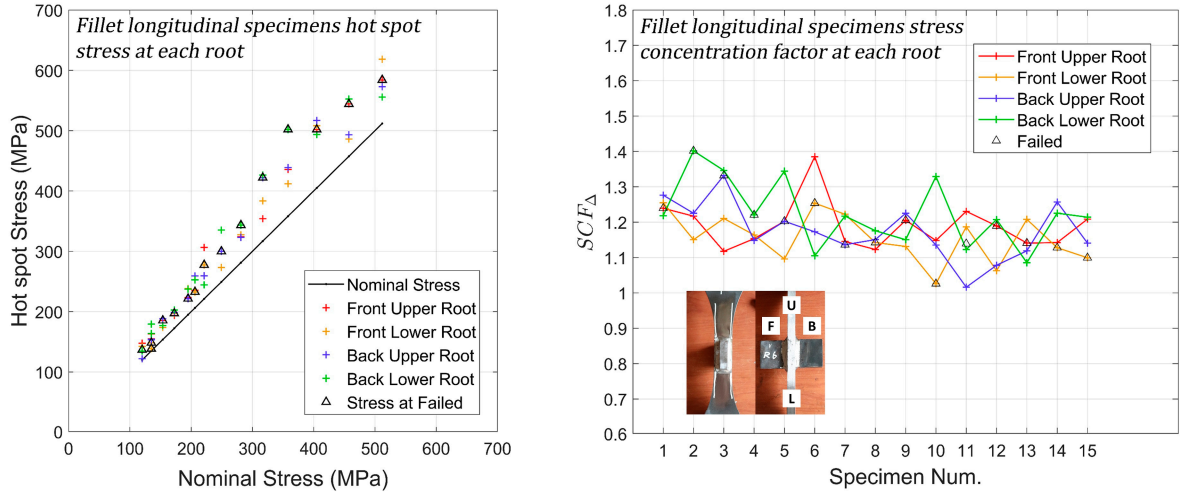
(**a**) (**b**)

Figure 21. Butt-welded specimens' fracture point information from room temperature tests. (**a**) Hot-spot stress at each root; (**b**) SCF_Δ at each root.



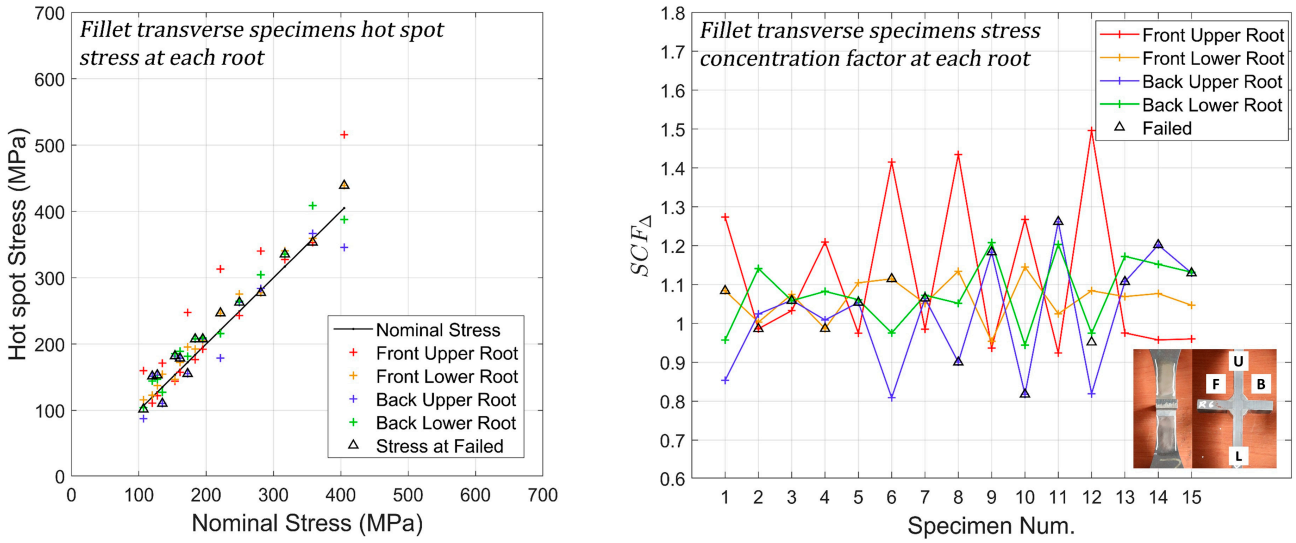
(**a**) (**b**) (**c**)

Figure 22. Fillet longitudinal specimen orientation. (**a**) U and L distinction; (**b**) F and B distinction; (**c**) total orientation.



(**a**) (**b**)

Figure 23. Fillet longitudinal specimens' fracture point information from room temperature tests. (**a**) Hot-spot stress at each root; (**b**) SCF_Δ at each root.

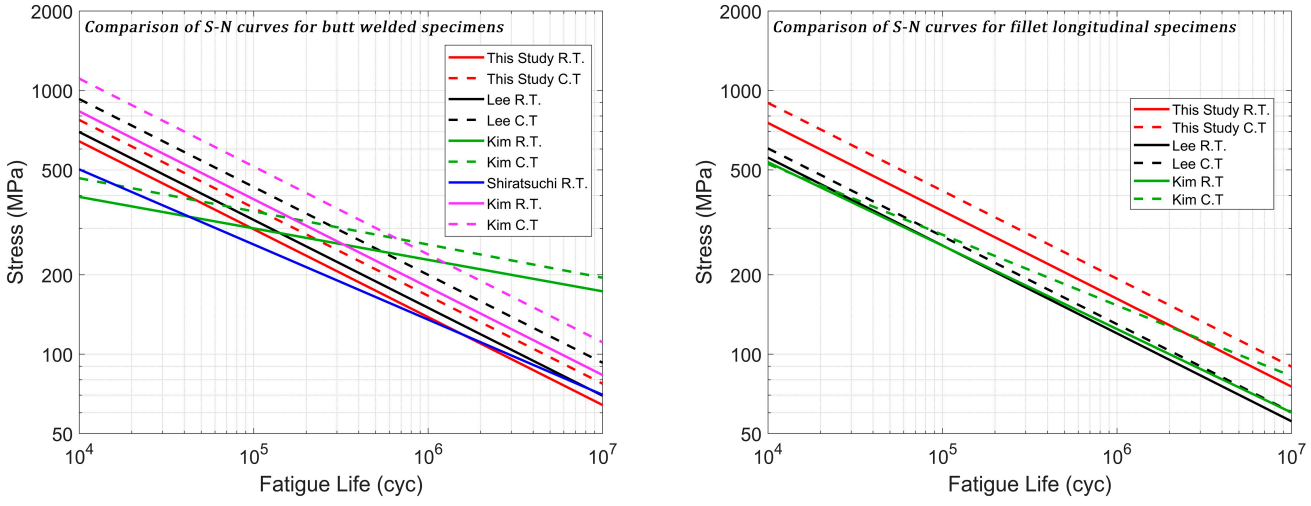


(**a**) (**b**)

Figure 24. Fillet transverse specimens' fracture point information from room temperature tests. (**a**) Hot-spot stress at each root; (**b**) SCF_Δ at each root.

4.4. Comparison of the S-N Curve

As for fatigue tests of 9% Ni steel, butt-welded and fillet longitudinal specimens had been reported in many studies [6–9]. Although the base metal is the same, the nominal stress-based S-N curve of the specimen will be different under different welding conditions, thicknesses, or stress ratios, as illustrated in Figure 25 and Table 5, respectively. The curves obtained in different studies are not identical. This research attributes the differences to the followings: (1) The stress concentration is different. (2) The welding process is different. (3) The stress range selected for the tests is different.



(**a**) (**b**)

Figure 25. Comparing the nominal stress-based S-N curve in references at room temperature (R.T.) with that at cryogenic temperature (C.T.). (**a**) Butt-welded specimens; (**b**) fillet longitudinal specimens.

Table 5. The S-N curve parameter summary and comparison.

	Author	Parameters (Mean Curve)	Butt-Welded	Fillet Longitudinal	Fillet Transverse	Thickness (mm)	Stress Ratio
Room Temperature	This Study	*loga*	28.60	29.08	28.58	12	0.1
		m	3	3	3		
		FAT	109.7	128.8	108.8		
	Lee et al. Adapted from Ref. [6]	*loga*	28.85	28.18	/	12	0
		m	3	3	/		
		FAT	119.0	95.2	/		
	Kim et al. Adapted from Ref. [7]	*loga*	59.31	29.06	/	12	0
		m	8.38	3.16	/		
		FAT	209.8	100.0	/		
	Shiratsuchi and Osawa Adapted from Ref. [8]	*loga*	31.01	/	/	22	0.05
		m	3.51	/	/		
		FAT	111.0	/	/		
	Kim et al. Adapted from Ref. [9]	*loga*	29.39	/	/	8	0.1
		m	3	/	/		
		FAT	142.5	/	/		
Cryogenic Temperature	This Study	*loga*	29.26	29.47	28.87	12	0.1
		m	3	3	3		
		FAT	132.2	153.4	115.4		
	Lee et al. Adapted from Ref. [6]	*loga*	29.18	28.42	/	12	0
		m	3	3	/		
		FAT	158.6	103.1	/		
	Kim et al. Adapted from Ref. [7]	*loga*	58.03	32.58	/	12	0
		m	7.95	3.73	/		
		FAT	238.8	127.1	/		
	Kim et al. Adapted from Ref. [9]	*loga*	30.24	/	/	8	0.1
		m	3	/	/		
		FAT	189.7	/	/		

Note: a, m = fatigue life curve parameters, *FAT* = the corresponding stress on the curve when fatigue life $N = 2 \times 10^6$ (cycles).

5. Discussion of Butt-Welded Test Results

5.1. Hot-Spot Stress Prediction

The SCF_Δ can be predicted according to Equation (13). In this section, the predicted SCF_Δ will be compared with the experimentally measured SCF_Δ. To evaluate the accuracy of predicting the SCF_Δ, the prediction error is defined as in Equation (23).

$$Er_i = \left(SCF_{\Delta,pred,i} - SCF_{\Delta,test,i}\right) / SCF_{test,i} \quad (23)$$

where the following apply:

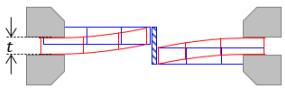
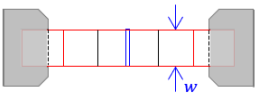
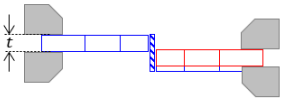
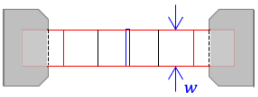
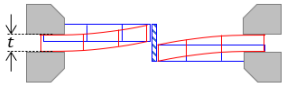
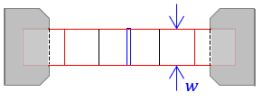
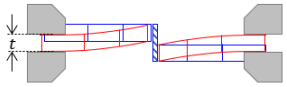
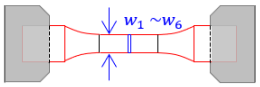
$SCF_{\Delta,pred,i}$: SCF_Δ from prediction;

$SCF_{\Delta,test,i}$: SCF_Δ from the test result;

i: specimen number.

In this part, only the room temperature test specimens are used for comparison. To obtain the k_{mis} and k_{ang}, four methods can be selected, which are summarized in Table 6.

Table 6. Four methods to calculate the misalignment-induced SCF.

Author	Contents		
BS 7910 Adapted from Ref. [29] and IIW Adapted from Ref. [30]	Classical method λ/t & $\lambda\alpha L/4t$		
DNV Adapted from Ref. [31]	Misalignment Tolerance $e_{cal} = e - 0.1t$		
Xing and Dong Adapted from Ref. [14]	Clamped effect		
This study	Clamped effect andNarrow mid-section		

Note: t = specimen thickness, L = specimen length, α = angular distortion, e = axial misalignment, e_{cal} = axial misalignment for calculation, λ = 3 for clamped and 6 for pinned condition, $w, w_{1\sim6}$ = specimen width.

As for considering the bead effect, three methods can be selected, which are summarized in Table 7. Method I represents the case which does not consider the bead effect. Method II assumes that $k_{bead,axil} = k_{bead,bend} = k_{axil,FE}$, which means that the influence of the bead on the axial stress and on the bending stress is the same. Method III considers the influence of the bead on the axial stress and on the bending stress, respectively, which is recommended in this study.

Table 7. Different ways to consider the bead effect.

Method	Contents		
	$k_{bead,axial}$ Value Selection	$k_{bead,bend}$ Value Selection	Formula
Method I	1	1	$SCF_{\Delta} = 1 + k_{mis} + k_{ang}$
Method II	$k_{axial,FE}$	$k_{axial,FE}$	$SCF_{\Delta} = k_{axial,FE}(1 + k_{mis} + k_{ang})$
Method III	$k_{axial,FE}$	$k_{bend,FE}$	$SCF_{\Delta} = k_{axial,FE} + k_{bend,FE}(k_{mis} + k_{ang})$

Note: $k_{axial,FE}$ = parameters of the bead effect under axial tension conditions obtained by FEM, $k_{bend,FE}$ = parameters of the bead effect under bending conditions obtained by FEM, k_{mis} = stress magnification factor due to axial misalignment, k_{ang} = stress magnification factor due to angular distortion.

First, compare the accuracy of predicting the SCF_{Δ} when different k_{mis} and k_{ang} prediction methods are applied. At this time, Method III is selected to consider the bead effect. When different prediction methods are employed, the prediction errors Er_i of each specimen at the different weld root positions are shown in Figure 26. Er_i = 0% means that the predicted SCF_{Δ} is exactly the same as the measured SCF_{Δ}. The positive value indicates an overestimation of the SCF_{Δ}, and the negative value indicates an underestimation.

To show the accuracy of the prediction more intuitively, take the average of $|Er_i|$ for all specimens, defined as Er_{ave}. As shown in Table 8, the method proposed in this study has higher accuracy than other methods. For the root FL with the highest probability of crack occurrence, the value of Er_{ave} is only 5.8%.

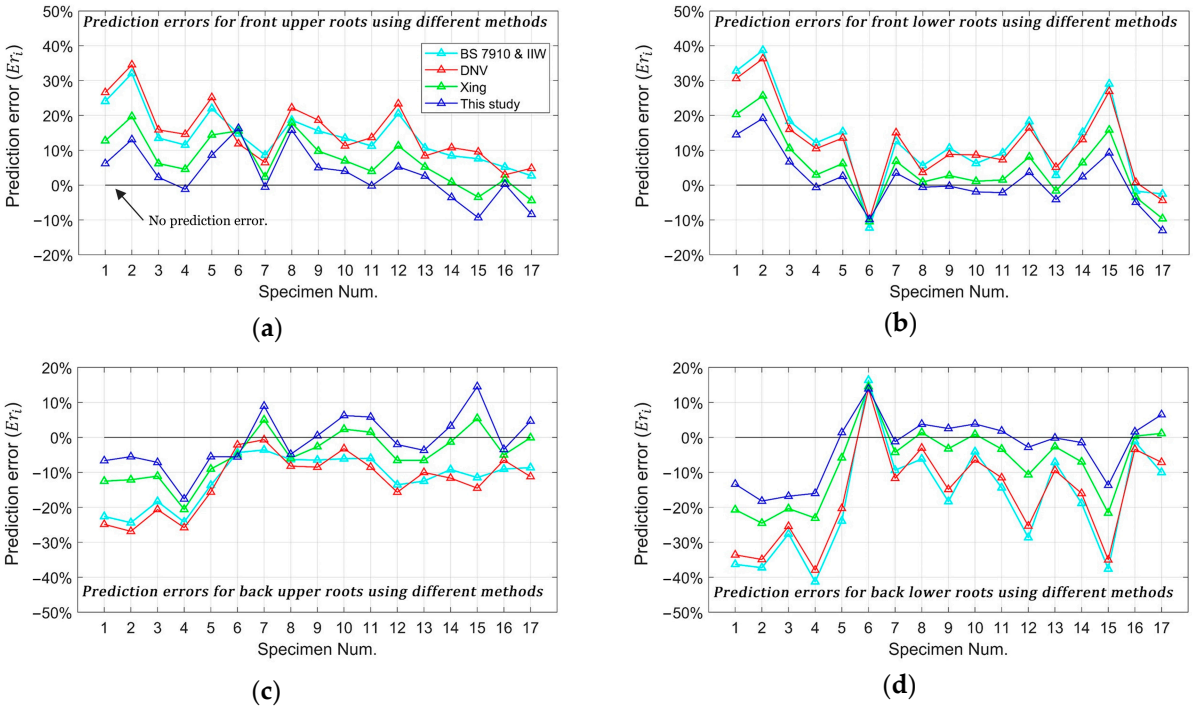


Figure 26. Comparison of accuracy when predicting misalignment effects using different methods. (**a**) Front upper roots; (**b**) front lower roots; (**c**) back upper roots; (**d**) back lower roots.

Table 8. Comparison of accuracy when predicting misalignment effects using different methods.

Er_{ave}	FU	FL	BU	BL	Average
BS 7910 and IIW	14.15%	14.32%	11.79%	19.91%	15.04%
DNV	15.34%	13.35%	12.62%	18.23%	14.89%
Xing	8.30%	7.90%	6.63%	9.73%	8.14%
This Study	6.03%	5.84%	6.23%	7.01%	6.28%
Number of crack occurrences	2/17	13/17	2/17	0/17	/S

Note: Er_{ave} = the average of the errors in the predicted results of all specimens at each root, FU = front upper root, FL = front lower root, BU = back upper root, BL = back lower root.

Next, the accuracy is compared when different methods are used to account for the bead effect. At this time, select the method proposed in this study to calculate k_{mis} and k_{ang}. The prediction errors Er_i for each specimen are given in Figure 27.

Table 9 indicates that the accuracy considering the bead effect is higher than that without considering the effect. If the effect of the bead on the axial stress and on the bending stress is investigated separately, the accuracy could be slightly improved. In addition to the physical meaning, according to the definition of $k_{bead,bend}$, it could be known from Equation (13) that $k_{bead,bend}$ could be used to describe the sensitivity of the specimen to the misalignment. So simply assuming that $k_{bead,bend}$ and $k_{bead,axial}$ are equal, like in Method II, is not rigorous. Due to the slight misalignment of the specimen used in this study, the prediction accuracy is not significantly improved when Method III is adopted.

Four ways could be used to calculate the k_{mis} and k_{ang}, and three ways could be selected when considering the bead effect. Therefore, there are a total of $4 \times 3 = 12$ methods to predict SCF_{Δ}. For each method, the mean Er_{ave} for each root can be calculated as $Er_{ave,4roots} = (Er_{ave,FU} + Er_{ave,4FL} + Er_{ave,BU} + Er_{ave,BL})/4$, summarized in Table 10.

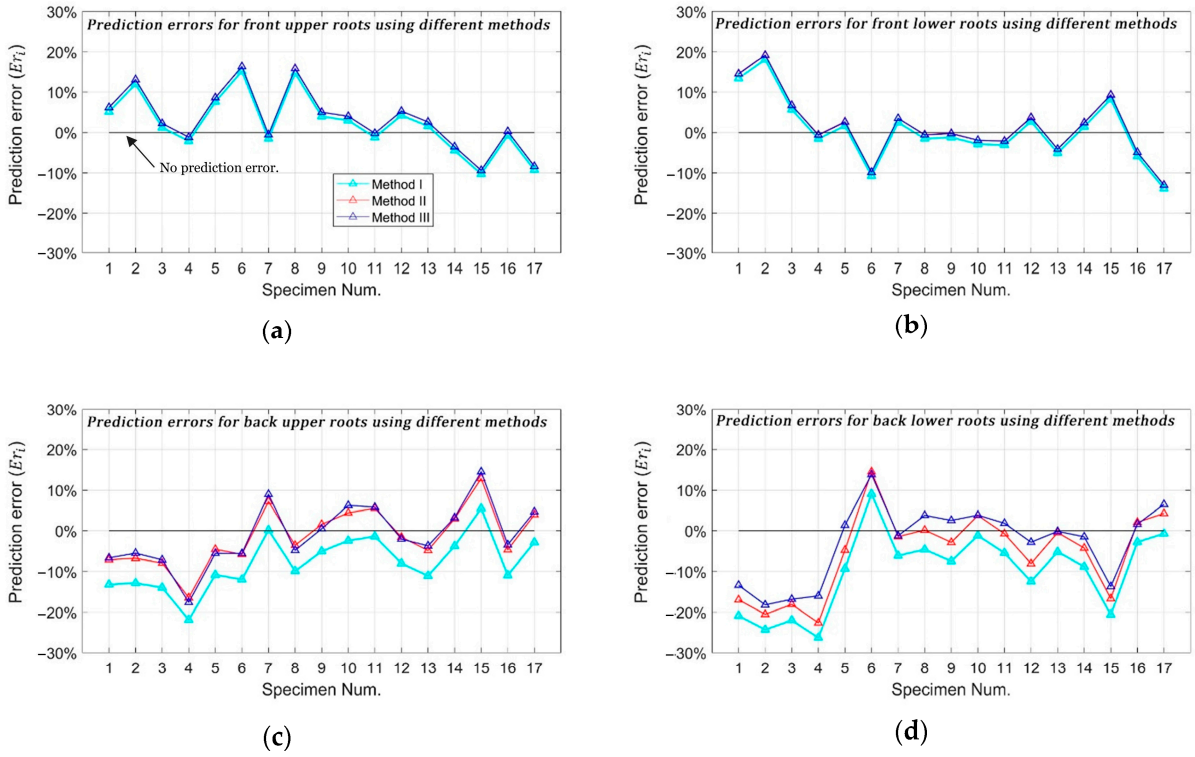


Figure 27. Comparison of accuracy when predicting bead effects using different methods. (**a**) Front upper roots; (**b**) front lower roots; (**c**) back upper roots; (**d**) back lower roots.

Table 9. Comparison of accuracy when predicting bead effects using different methods.

Er_{ave}	FU	FL	BU	BL	Average
Method I	5.77%	5.85%	8.57%	11.01%	7.80%
Method II	6.03%	5.85%	5.98%	8.36%	6.56%
Method III	6.03%	5.84%	6.23%	7.01%	6.28%
Number of crack occurrences	2/17	13/17	2/17	0/17	/

Note: Er_{ave} = the average of the errors in the predicted results of all specimens at each root, FU = front upper root, FL = front lower root, BU = back upper root, BL = back lower root.

Table 10. Comparing the accuracy of twelve different methods.

$Er_{ave,4roots}$		Different Ways to Consider the Bead Effect			Average
		Method I	Method II	Method III	
Different methods to calculate the k_{mis} and k_{ang}	BS 7910 and IIW	18.18%	16.48%	15.04%	16.32%
	DNV	18.45%	16.78%	14.89%	16.49%
	Xing	10.69%	8.84%	8.14%	9.02%
	This Study	7.80%	6.56%	6.28%	6.75%
Average		13.78%	12.16%	11.09%	-

Note: $Er_{ave,4\ roots}$ = the average of the errors in the predicted results of all specimens from four roots.

Table 10 indicates that using the proposed method in this study to calculate k_{mis} and k_{ang}, and considering the influence of the bead on the tensile and bending stress separately, the accuracy of predicting the SCF_{Δ} could be improved. The method proposed in this study to predict the stress concentration factor is depicted in Figure 28.

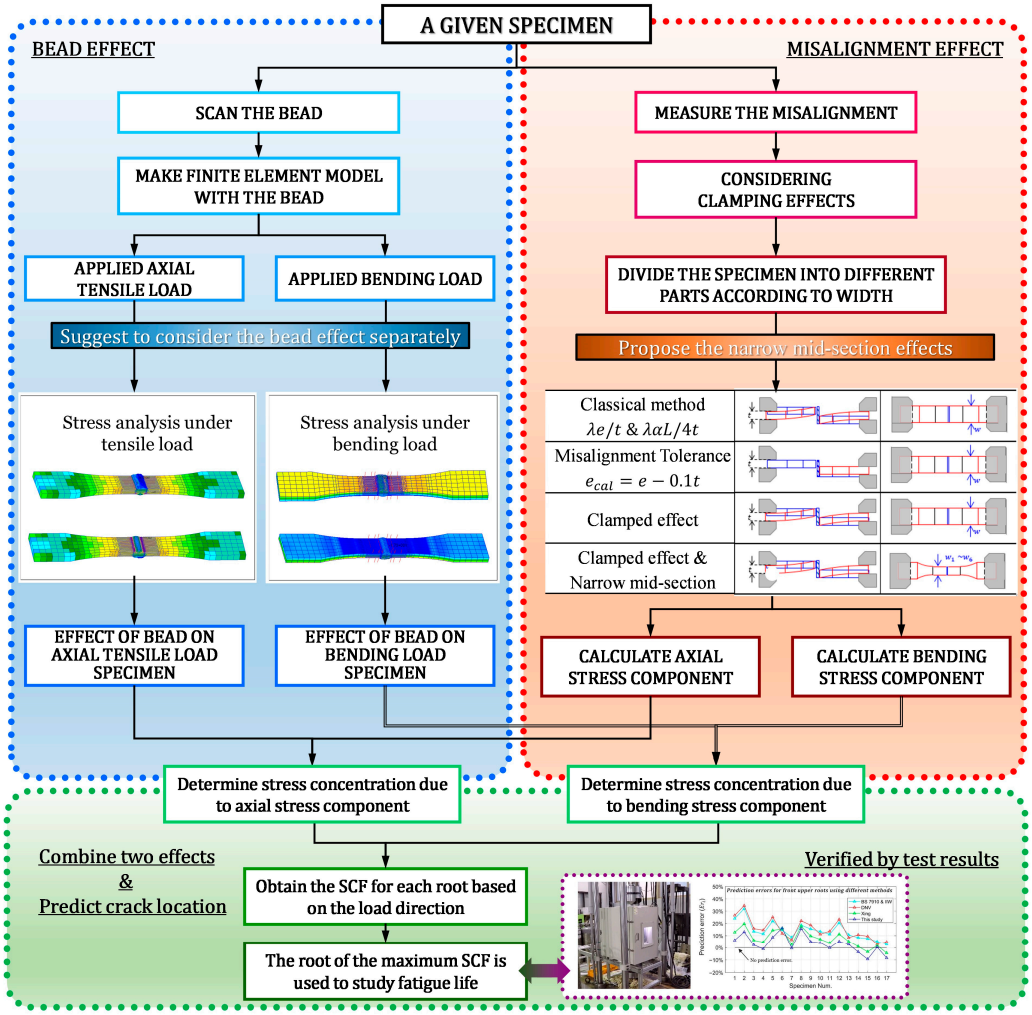


Figure 28. Method to predict the stress concentration factor for the butt specimen.

5.2. Predicted Hot-Spot Stress-Based S-N Curve

Using the predicted SCF_{Δ}, the S-N curve can be plotted based on the predicted hot-spot stress. The comparison results are shown in Figure 29.

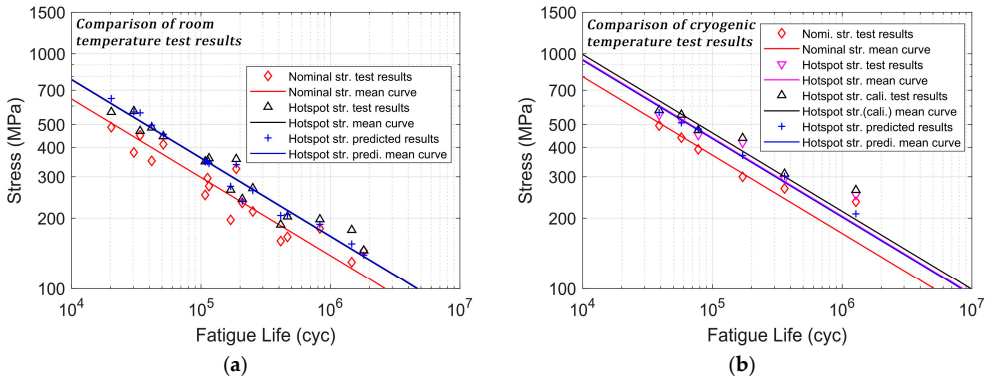


Figure 29. Comparison between the butt-welded specimen S-N curves. (**a**) Room temperature tests; (**b**) cryogenic temperature tests.

The predicted hot-spot stress-based S-N curve has a higher correlation coefficient than the nominal stress-based S-N curve, as shown in Table 11. The predicted hot-spot stress-based S-N curve is similar to the measured hot-spot stress-based S-N curve.

Table 11. Information about three S-N curves.

Butt-Welded Specimen			Room Temperature	Cryogenic Temperature
Nominal stress based	$\Delta\sigma_{nom} - N$	$loga$	28.60	29.26
		r^2	0.8897	0.9642
		FAT	109.7 (MPa)	136.7 (MPa)
Hot-spot stress-based (from the test)	$\Delta\sigma_{hs,test} - N$	$loga$	29.16	29.77
		r^2	0.9403	0.9174
		FAT	132.2 (MPa)	162.0 (MPa)
Hot-spot stress-based (from test and calibration)	$\Delta\sigma_{hs,cali} - N$	$loga$	/	29.91
		r^2	/	0.9174
		FAT	/	169.8 (MPa)
Hot-spot stress-based (from prediction)	$\Delta\sigma_{hs,pred} - N$	$loga$	29.18	29.74
		r^2	0.9719	0.9765
		FAT	133.0 (MPa)	160.4 (MPa)

Note: a = fatigue life curve parameter, r^2= correlation coefficient, N = fatigue life, FAT = the corresponding stress on the curve when fatigue life $N = 2 \times 10^6$ (cycles).

6. Conclusions

The present study provides the S-N curves for three kinds of welded specimens. To overcome the problems that may arise during the strain gauge measurement, this study proposes a hot-spot stress prediction method that considers multiple factors affecting hot-spot stress. The reliability of the prediction method is proved by comparing the predicted hot-spot stress with the experimentally measured hot-spot stress. The obtained outcomes can be summarized as follows:

1. To address potential issues during strain gauge measurements, the study proposes a hot-spot stress prediction method. This method considers multiple factors influencing hot-spot stress, enhancing the reliability of stress predictions. Experimental verification confirms the accuracy of predicted hot-spot stresses compared to measured values.
2. This study proposes an innovative approach focusing on the influence of the mid-section of the specimen on stress concentration factor (SCF) prediction. Taking into account the clamped effect and the reduced mid-section allows the obtained k_{mis}, k_{ang} values to more accurately predict the hot-spot stress.
3. The bead is found to have different effects on the axial tensile stress and on the bending stress concentration. By considering the effect of the bead on axial nominal stress and on bending stress separately, the prediction accuracy can also be improved.
4. The research discovers that the ratio of output strain between 3-wire and 2-wire strain gauges remains constant. This finding allows for the correction of 2-wire strain gauge outputs in cryogenic environments, thereby improving the accuracy of experimental results.

The limitation of this study is that the effect of residual stress on fatigue life is not considered. Whether k_{bead} is affected by the thickness, and whether it can be applied to more specimens, remains to be investigated. Future studies could address these limitations to enhance understanding and application.

Author Contributions: Conceptualization, Y.-Y.L. and Y.-H.P.; methodology, Y.-Y.L. and D.K.K.; software, S.-W.H. and Y.-Y.L.; validation, Y.-Y.L. and D.K.K.; formal analysis, Y.-Y.L. and D.K.K.; investigation, S.-W.H. and Y.-Y.L.; resources, Y.-H.P.; data curation, Y.-Y.L. and D.K.K.; writing—original draft preparation, Y.-Y.L. and D.K.K.; writing—review and editing, Y.-Y.L. and D.K.K.; visualization,

Y.-Y.L. and D.K.K.; supervision, D.K.K.; project administration, Y.-H.P.; funding acquisition, Y.-H.P. All authors have read and agreed to the published version of the manuscript.

Funding: The present research was made possible by the project "Experimental study on material and fatigue for 9% Ni Steel at cryogenic temperature" (project no. 0457-20200025) supported by POSCO. This work was also supported by a research project (P0018490, Development of Performance Evaluation Technics for LNG Cryogenic Cargo Containment Material and Structure System) funded by the Ministry of Trade, Industry & Energy (MOTIE, Korea). The APC was funded by *Metals* journal.

Data Availability Statement: The raw data supporting the conclusions of this article will be made available by the authors on request.

Acknowledgments: All the authors wish to extend their profound gratitude to the late Beom-Seon Jang, whose exceptional dedication and technical expertise were indispensable to the success of this research. Thank you.

Conflicts of Interest: Author Young-Hwan Park was employed by the company POSCO. The remaining authors declare that the research was conducted in the absence of any commercial or financial relationships that could be construed as a potential conflict of interest.

Abbreviations

Er_{ave}	Average of SCF_{Δ} prediction errors of all specimens at each root
$Er_{ave,4roots}$	Average of SCF_{Δ} prediction errors of all specimens from four roots
Er_i	SCF_{Δ} prediction error for i_{th} specimen
FAT	The corresponding stress on the curve when fatigue life $N = 2 \times 10^6$ (cycles)
K	Gauge factor
$K_{2w/3w,room/cryo}$	2-/3-wire strain gauge factor in room/cryogenic temperature
L/L_i	The total length of the specimen/length of each part of the specimen $(i = 1 \sim 6)$
M	Mean curve
$M - 2STD$	Design curve
$R_{2w/3w,Gr}$	2-/3-wire strain gauge grid resistance
R_G	Gauge resistance
R_{Gr}	Gauge grid resistance
R_W	Gauge wire resistance
SCF	Stress concentration factor
SCF_{Δ}	Stress concentration factor when focusing on the loading range
$SCF_{\Delta,pred}$	SCF_{Δ} from prediction
$SCF_{\Delta,test}$	SCF_{Δ} from the test
a/m	Fatigue life curve parameters
e	Axial misalignment
e_{cal}	The axial misalignment used to calculate SCF in DNV
k_{ang}	Stress magnification factor due to angular distortion
$k_{axial/bend,FE}$	Stress magnification factor due to the bead from axial tensile/bending FE model
k_{bead}	Stress magnification factor due to the bead
$k_{bend,FE}$	Stress magnification factor due to the bead from bending FE model
k_{mis}	Stress magnification factor due to axial misalignment
r^2	Correlation coefficient
std	Standard deviation
t	Thickness
w/w_i	Width of the specimen/width of each part of the specimen$(i = 1 \sim 6)$
ΔR_{Gr}	Change in resistance of the gauge grid due to deformation of attached object
$\Delta\sigma_{hs}$	Hot-spot stress range
$\Delta\sigma_{hs,cali}$	Hot-spot stress range from the test after calibration
$\Delta\sigma_{hs,pred}$	Hot-spot stress range from prediction
$\Delta\sigma_{hs,test}$	Hot-spot stress range from the test
$\Delta\sigma_{axial}$	Nominal stress for balanced axial load in specimen
$\Delta\sigma_{bend}$	Bending stress range due to misalignment

$\Delta\sigma_{bend,ang}$	Bending stresses for balanced moment in angular distortion existed specimen
$\Delta\sigma_{bend,mis}$	Bending stresses for balanced moment in axial misalignment existed specimen
$\Delta\sigma_{nom}$	Nominal stress range
α	Angular distortion
ε	Strain
$\varepsilon_{2w,cryo,ac/inac}$	Strain measured at cryogenic temperature by the 2-wire strain gauge, if accurate/inaccurate gauge factor is used
$\varepsilon_{2w/3w,room/cryo}$	Strain measured by the 2-/3-wire strain gauge at room/cryogenic temperature
σ_{hs}	Hot-spot stress
$\sigma_{hs,axial/bend,FE}$	Hot-spot stress obtained from the FE model when axial tensile/bending stress is applied
$\sigma_{hs,grip}$	Hot-spot stress initiated by gripping
$\sigma_{hs,nom}$	Hot-spot stress initiated by nominal stress
σ_{grip}	Nominal bending stress induced by gripping
σ_{nom}	Nominal stress
$\sigma_{nom,axial/bend,FE}$	The applied nominal axial tensile/bending stress when studying the bead effect

Appendix A

Specimens are made along the transverse and longitudinal direction of the base metal. Both longitudinal and transverse specimens are tested at room temperature and cryogenic temperature. The dimensions are shown in Figure A1. The specimen dimensions and test procedures follow the ASTM standard [34].

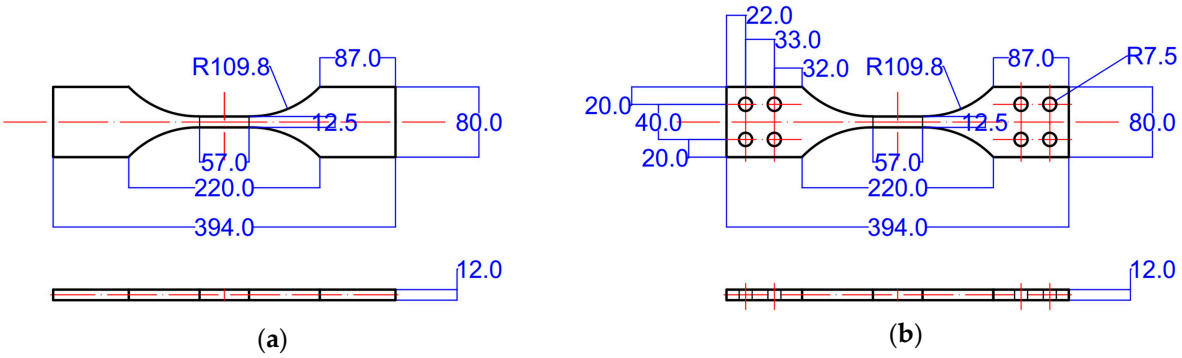


Figure A1. Monotonic test specimen dimensions (unit: mm). (**a**) Room temperature test specimen; (**b**) cryogenic temperature test specimen.

The stress–strain curves are shown in Figure A2, and material properties are given in Table A1.

Table A1. Monotonic tensile test results.

Temperature	*E* (GPa)	Yield				Tensile		Fracture	
		Upper		Lower					
		Strength (MPa)	Strain (mm/mm)	Strength (MPa)	Strain (mm/mm)	Strength (MPa)	Strain (mm/mm)	Strength (MPa)	Strain (mm/mm)
Cryogenic (−163 °C)	204.9	796.9	0.49%	790.2	0.85%	951.4	14.34%	629.6	31.24%
Room (20 °C)	197.3	670.3	0.40%	654.2	1.53%	716.4	10.97%	438.7	30.31%

The Young's modulus (*E*) of 9%Ni steel increases with decreasing temperature. The yield strength, tensile strength, and fracture strength are significantly increased, and the corresponding strain increased slightly.

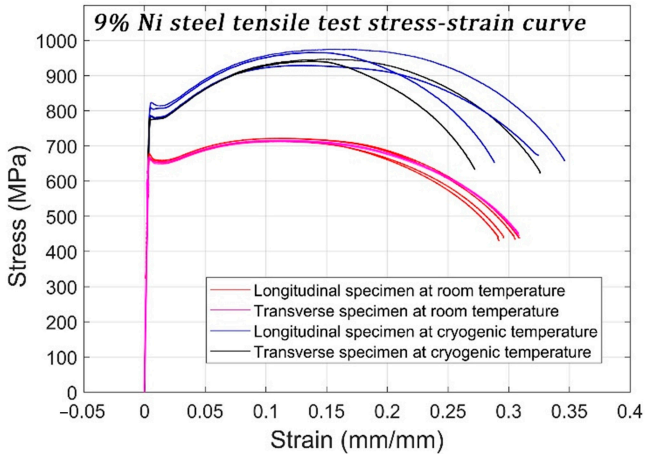


Figure A2. Monotonic tensile test stress–strain curve.

References

1. Serindağ, H.T.; Tardu, C.; Kirçiçek, İ.Ö.; Çam, G. A study on microstructural and mechanical properties of gas tungsten arc welded thick cryogenic 9% Ni alloy steel butt joint. *CIRP J. Manuf. Sci. Technol.* **2022**, *37*, 1–10. [CrossRef]
2. MEPC. Amendments to the Annex of the Protocol of 1997 to Amend the International Convention for the Prevention of Pollution From Ships, 1973, as Modified by the Protocol of 1978 Relating Thereto. In *Amendments to MARPOL Annex VI*; MEPC: London, UK, 2011; Volume 70, p. 18.
3. Abdussamie, N.; Daboos, M.; Elferjani, I.; Shuhong, C.; Alaktiwi, A. Risk assessment of LNG and FLNG vessels during manoeuvring in open sea. *J. Ocean Eng. Sci.* **2018**, *3*, 56–66. [CrossRef]
4. Cao, Y.; Jia, Q.J.; Wang, S.M.; Jiang, Y.; Bai, Y. Safety design analysis of a vent mast on a LNG powered ship during a low-temperature combustible gas leakage accident. *J. Ocean Eng. Sci.* **2022**, *7*, 75–83. [CrossRef]
5. Oh, D.J.; Lee, J.M.; Noh, B.J.; Kim, W.S.; Ryuichi-Ando; Toshiyuki-Matsumoto; Kim, M.H. Investigation of fatigue performance of low temperature alloys for liquefied natural gas storage tanks. *Proc. Inst. Mech. Eng. Part C-J. Eng. Mech. Eng. Sci.* **2015**, *229*, 1300–1314. [CrossRef]
6. Lee, J.S.; You, W.H.; Yoo, C.H.; Kim, K.S.; Kim, Y. An experimental study on fatigue performance of cryogenic metallic materials for IMO type B tank. *Int. J. Nav. Archit. Ocean Eng.* **2013**, *5*, 580–597. [CrossRef]
7. Kim, Y.W.; Oh, D.J.; Lee, J.M.; Noh, B.J.; Sung, H.J.; Ando, R.; Matsumoto, T.; Kim, M.H. An experimental study for fatigue performance of 7% nickel steels for type b liquefied natural gas carriers. *J. Offshore Mech. Arct. Eng.* **2016**, *138*, 031401. [CrossRef]
8. Shiratsuchi, T.; Osawa, N. Fatigue life prediction for 9% Ni steel butt welded joints. *Int. J. Fatigue* **2021**, *142*, 105925. [CrossRef]
9. Kim, T.Y.; Yoon, S.W.; Kim, J.H.; Kim, M.H. Fatigue and Fracture Behavior of Cryogenic Materials Applied to LNG Fuel Storage Tanks for Coastal Ships. *Metals* **2021**, *11*, 1899. [CrossRef]
10. Saini, D.S.; Karmakar, D.; Ray-Chaudhuri, S. A review of stress concentration factors in tubular and non-tubular joints for design of offshore installations. *J. Ocean Eng. Sci.* **2016**, *1*, 186–202. [CrossRef]
11. Dong, Y.; Teixeira, A.P.; Soares, C.G. Fatigue reliability analysis of butt welded joints with misalignments based on hotspot stress approach. *Mar. Struct.* **2019**, *65*, 215–228. [CrossRef]
12. Xin, H.; Correia, J.A.F.O.; Veljkovic, M.; Berto, F.; Manuel, L. Residual stress effects on fatigue life prediction using hardness measurements for butt-welded joints made of high strength steels. *Int. J. Fatigue* **2021**, *147*, 106175. [CrossRef]
13. Kim, M.H.; Kim, S.M.; Kim, Y.N.; Kim, S.G.; Lee, K.E.; Kim, G.R. A comparative study for the fatigue assessment of a ship structure by use of hot spot stress and structural stress approaches. *Ocean Eng.* **2009**, *36*, 1067–1072. [CrossRef]
14. Xing, S.; Dong, P. An analytical SCF solution method for joint misalignments and application in fatigue test data interpretation. *Mar. Struct.* **2016**, *50*, 143–161. [CrossRef]
15. Berge, S.; Myhre, H. Fatigue strength of misaligned cruciform and butt joints. *Norw. Mar. Res.* **1977**, *5*, 29–39.
16. Braun, M.; Kellner, L.; Schreiber, S.; Ehlers, S. Prediction of fatigue failure in small-scale butt-welded joints with explainable machine learning. *Procedia Struct. Integr.* **2022**, *38*, 182–191. [CrossRef]
17. Chen, Z.; Yu, B.; Wang, P.; Qian, H.; Dong, P. Fatigue behaviors of aluminum alloy butt joints with backing plates: Experimental testing and traction stress modeling. *Int. J. Fatigue* **2022**, *163*, 107040. [CrossRef]
18. Qiu, Y.; Shen, W.; Yan, R.; Xu, L.; Liu, E. Fatigue reliability evaluation of thin plate welded joints considering initial welding deformation. *Ocean Eng.* **2021**, *236*, 109440. [CrossRef]
19. Cui, W.; Wan, Z.; Mansour, A.E. Stress concentration factor in plates with transverse butt-weld misalignment. *J. Constr. Steel. Res.* **1999**, *52*, 159–170. [CrossRef]
20. Kang, S.W.; Park, Y.M.; Jang, B.S.; Jeon, Y.C.; Kim, S.M. Study on fatigue experiment for transverse butt welds under 2G and 3G weld positions. *Int. J. Nav. Archit. Ocean Eng.* **2015**, *7*, 833–847. [CrossRef]

21. Lillemäe, I.; Lammi, H.; Molter, L.; Remes, H. Fatigue strength of welded butt joints in thin and slender specimens. *Int. J. Fatigue* **2012**, *44*, 98–106. [CrossRef]
22. Mashiri, F.R.; Zhao, X.L.; Grundy, P. Effects of weld profile and undercut on fatigue crack propagation life of thin-walled cruciform joint. *Thin-Walled Struct.* **2001**, *39*, 261–285. [CrossRef]
23. Hong, K.; Oterkus, S.; Oterkus, E. Peridynamic analysis of fatigue crack growth in fillet welded joints. *Ocean Eng.* **2021**, *235*, 109348. [CrossRef]
24. Chen, Z.; Yu, B.; Wang, P.; Qian, H. Fatigue properties evaluation of fillet weld joints in full-scale steel marine structures. *Ocean Eng.* **2023**, *270*, 113651. [CrossRef]
25. Xing, S.; Pei, X.; Mei, J.; Dong, P.; Su, S.; Zhen, C. Weld toe versus root fatigue failure mode and governing parameters: A study of aluminum alloy load-carrying fillet joints. *Mar. Struct.* **2023**, *88*, 103344. [CrossRef]
26. Ahola, A.; Björk, T. Fatigue strength of misaligned non-load-carrying cruciform joints made of ultra-high-strength steel. *J. Constr. Steel. Res.* **2020**, *175*, 106334. [CrossRef]
27. Skriko, T.; Ahola, A.; Poutiainen, I.; Björk, T. Fatigue strength of laser-dressed non-load-carrying fillet weld joints made of ultra-high-strength steel. *Procedia Struct. Integr.* **2022**, *38*, 393–400. [CrossRef]
28. *BS 7910*; Guide to Methods for Assessing the Acceptability of Flaws in Metallic Structures. British Standard: London, UK, 2015. [CrossRef]
29. Hobbacher, A. *Recommendations for Fatigue Design of Welded Joints and Components*; IIW (International Institute of Welding): Paris, France, 2018. [CrossRef]
30. DNV. Fatigue design of offshore steel structures. In *DNV Recommended Practice (DNV-RP-C203)*; DNV: Oslo, Norway, 2010.
31. Shen, W.; Qiu, Y.; Xu, L.; Song, L. Stress concentration effect of thin plate joints considering welding defects. *Ocean Eng.* **2019**, *184*, 273–288. [CrossRef]
32. *ASTM E466*; Standard Practice for Conducting Force Controlled Constant Amplitude Axial Fatigue Tests of Metallic Materials. ASTM International: West Conshohocken, PA, USA, 2015. [CrossRef]
33. Hannah, R.; Reed, S.E. *Strain Gage Users' Handbook*; Springer Science & Business Media: Berlin/Heidelberg, Germany, 1992.
34. *ASTM E8/E8M*; Standard Test Methods for Tension Testing of Metallic Materials. ASTM International: West Conshohocken, PA, USA, 2014. [CrossRef]

Disclaimer/Publisher's Note: The statements, opinions and data contained in all publications are solely those of the individual author(s) and contributor(s) and not of MDPI and/or the editor(s). MDPI and/or the editor(s) disclaim responsibility for any injury to people or property resulting from any ideas, methods, instructions or products referred to in the content.